LaCoDe: a Lagrangian two-dimensional thermo-mechanical code for large-strain compressible visco-elastic geodynamical modeling

Albert de Montserrat[a], Jason P. Morgan[b], Jörg Hasenclever[c]

[a] *SE Asia Research Group, Department of Earth Sciences, Royal Holloway University of London, Egham, United Kingdom*
[b] *Royal Holloway University of London, Department of Earth Sciences, Egham, United Kingdom*
[c] *Institute of Geophysics, Hamburg University, Hamburg, Germany*

Abstract

We present LaCoDe (Lagrangian Compressible Deformation), a MATLAB solver for the Stokes equations for compressible non-Newtonian visco-elastic in two dimensions, based on a Lagrangian formulation of the Finite Element Method. The incompressible Boussinesq approximation is a widespread assumption in numerical models of lithospheric deformation, thus potentially masking a significant contribution of mechanisms linked to volumetric changes that occur in the asthenospheric mantle and the lithosphere. LaCoDe employs a compressible formulation of the Stokes equations designed to address such volume-changing processes. First, we provide a description of the equations governing the deformation of Earth rocks and detailed overview of the algorithm, its numerical implementation, treatment of the non-linearities rising from the compressible formulation, and the remeshing algorithm that tracks and transfers the physical fields that describe the material deformation from a highly-distorted to a high-quality mesh. LaCoDe is then benchmarked by comparing numerical results to analytical solutions for the bending of a thin elastic beam under a constant uniform load, flow around a rigid inclusion, Rayleigh-Taylor instability, stress build-up in a visco-elastic Maxwell body, and Couette flow with viscous heating. The Rayleigh-Taylor instability test is further used to demonstrate the accuracy of the remeshing algorithm. The importance of including volumetric strain for geodynamic processes is illustrated by two numerical experiments: i) volumetric-strain inducing phase changes in amagmatic slow-spreading ridges, and ii) subducting slabs.

Keywords:
Numerical geodynamic modeling, Compressible formulation, Finite Element Method, Large-strain deformation, Visco-elastic rheology

1. Introduction

Rocks are exposed to thermal, mechanical and chemical processes that induce volumetric changes. Obvious examples are mechanical compression and decompression, thermal expansion, and phase changes resulting from partial melting and serpentinisation. Even though stresses related to compressibility may play an important role in rock deformation and failure, the incompressible Boussinesq approximation of the governing equations is the most common approach used in geodynamic modeling of coupled asthenosphe-lithosphere systems. This approximation is considered to be reasonably valid under lithospheric conditions and offers a simple and straightforward numerical implementation, hence its popularity. The Boussinesq approximation has been considered to be appropriate if: 1) the density of the material does not change more than 10% with respect to its reference value (Spiegel and Veronis, 1959; Gray and Giorgini, 1976); and, 2) volume-change-related stresses are small with respect to the hydrostatic pressure and deformation-linked stresses.

These approximations are usually valid for lithosphere-scale models, but may be violated in certain scenarios. For instance, it is well known that metamorphic phase changes occurring at crustal conditions can induce significant changes in density in localised regions that far exceed the maximum density changes thought to be appropriate for the Boussinesq approximation. In the case of partial serpentinisation, for example, density can be reduced by 18% or more, and its associated volumetric strain can cause rocks to fail. This mechanism potentially reduces the strength of the lithosphere by 30% (Escartin et al., 1997), or even more when intact rock is replaced by a serpentinised fault. Volume-change-linked stresses related to phase changes may therefore have a significant influence on the localisation of deformation when brittle failure is an important rheological feature.

The first studies proposing a compressible formulation for mantle deformation (Jarvis and McKenzie, 1980; Quareni et al., 1986; Yuen et al., 1987) made use of the so-called anelastic approximation. These studies aimed at understanding the behaviour of deep mantle convection; implications for lithospheric failure and deformation were not considered. In the last decades numerous studies focused on the development of numerical tools to investigate lithospheric and upper mantle geodynamical processes (e.g. Christensen, 1987; Braun and Sambridge, 1994; Fullsack, 1995; Schmalholz et al., 2001; Moresi et al., 2003; Petrunin and Sobolev, 2006; Gerya and Yuen, 2007; von Tscharner and Schmalholz, 2015). However, all of these studies assumed the Boussinesq incompressible approximation. To date, relatively little effort has been made to include and discuss the effects of volumetric strain at the lithospheric scale. To our knowledge, SLIM3D (Popov and Sobolev, 2008) and DynEarthSol2D (Choi et al., 2013) are the only available numerical models that include elastic compressibility. However, these studies do not assess its implications for lithospheric scale processes.

We propose a new compressible formulation that has been implemented in the new 2-D geodynamic code LaCoDe, which is based on the incompressible code M2TRI (Hasenclever, 2010; Hasenclever et al., 2011). LaCoDe solves for visco-elastic deformation, thermal convection and melting processes, in a Lagrangian frame of reference. It is written in MATLAB and uses an optimised matrix assembly based on the 'blocking' and vectorisation techniques described in Dabrowski et al. (2008). Stokes equations are solved using a Lagrangian mixed velocity-pressure approach with the Finite Element Method (FEM). An additional feature of LaCoDe, not discussed here, is a free-surface algorithm (Andrés-Martínez et al., 2015) that allows improved tracking of the evolution of topographic relief.

The primary purpose of this paper is to assess the stability of the numerical implementation of a visco-elastic rheology that does not assume the incompressible Boussinesq approximation and to emphasize its relevance for modeling geological events at the scale of the lithosphere. We first describe the new formulation and its numerical implementation. We then test the accuracy of the code with a series of benchmarks for viscous and elastic deformation for which analytical solution is known: i) bending of a thin beam under a distributed load; the ii) SolCx and iii) SolKz tests (Duretz et al., 2011); iv) deformation around a viscous inclusion; v) Rayleigh-Taylor instability; vi) stress build-up in a visco-elastic Maxwell body; and vii) solution of a Couette-flow with viscous heating and temperature-dependent viscosity. Following these benchmarks, we demonstrate that nested Picard iterations are the most cost-effective scheme to deal with the combination of non-linear rheologies and a compressible formulation. Finally, we show two examples of tectonic processes where volumetric strain potentially plays a key role: i) volumetric strain linked to phase changes, and ii) comparison between subduction of a compressible and incompressible slab.

2. Governing equations for compressible flow

Mantle-lithosphere deformation is treated as a thermo-mechanical process described by the equations of conservation of momentum, conservation of mass, and conservation of energy in a domain Ω, respectively:

$$\frac{\partial \sigma_{ij}}{\partial x_j} = -\rho g_i \tag{1}$$

$$\frac{D\rho}{Dt} + \rho \frac{\partial u_i}{\partial x_i} = q_m \tag{2}$$

$$\rho C_p \frac{DT}{Dt} = \frac{\partial}{\partial x_i}\left(\kappa \frac{\partial T}{\partial x_i}\right) + \alpha T \frac{Dp}{Dt} + H_q + H_{sh} \tag{3}$$

where ρ is the density, x_i are the spatial coordinates, u_i are the velocity components, σ_{ij} is the Cauchy stress tensor, g_i is the gravitational acceleration, C_p

is the heat capacity, T is the temperature, κ is the thermal conductivity, α is the thermal expansivity, $\alpha T Dp/Dt$ is the adiabatic heating, H_r is a heat production rate, and shear heating is defined as the energy released by the inelastic work $H_{sh} = \sigma_{ij}\varepsilon_{ij}^{inel}$, and t is time. The subscripts i and j refer to the horizontal and vertical directions in a two-dimensional Cartesian coordinate system, respectively. The function $q_m = q(x,t)$ in eq. (2) describes the rate of mass being added (local source of mass: $q_m > 0$) or subtracted (local sink of mass: $q_m < 0$) from a region, with dimensions of mass per unit volume and unit time. Note that, when a Lagrangian frame of reference is adopted, the material time derivative $D(\cdot)/Dt$ is equal to the partial time derivative $\partial(\cdot)/\partial t$.

The set of equations (1), (2) and (3) describe the thermo-mechanical behavior of compressible viscous flow. Several approximations of these equations have been widely employed to address the effects of compressibility within the mantle, such as the anelastic approximation (ALA) or the truncated anelastic approximation (TALA) (e.g. Jarvis and McKenzie, 1980; Bercovici et al., 1992; King et al., 2010; Heister et al., 2017). On the other hand, models studying geodynamic processes at a lithosphe scale (e.g. from rifting of continental crust, to subducting slabs) widely employ the so-called incompressible Boussinesq approximation, where the continuity equation is approximated as being divergence-free. In the (T)ALA approximations the dynamic pressure is assumed to be negligible with respect to the hydrostatic pressure ($p_{dyn} << p_{total}$), leading to a depth-dependent formulation for density. However, dynamic pressure effects could also become locally significant in tectonic processes such as subducting slabs or during phase changes. Therefore, we chose a more complete formulation in which the dynamic pressure is taken into consideration and employ an equation of state that depends on the total pressure:

$$\rho(T,p) = \rho_o\left[1 - \alpha(T - T_o) + K^{-1}(p - p_o)\right] \tag{4}$$

where ρ_o, T_o, p_o are the reference density, temperature and pressure, respectively, K is the bulk modulus and p is total pressure. It is convenient to define a reference density so that additional volumetric changes are determined as a further deviation from this reference state. In this paper, we are the lithostatic pressure to define the reference density profile. If one wishes, density changes due to phase changes can also be incorporated into the equation of state.

2.1. Mixed formulation

The implementation of a mixed formulation to solve the Stokes equations splits the Cauchy stress tensor into its deviatoric and pressure components:

$$\sigma_{ij} = \tau_{ij} - p\delta_{ij} \tag{5}$$

where τ_{ij} is the deviatoric stress tensor, δ_{ij} is the Kroenecker delta, and the pressure is the mean of the principal stresses $p = -\sigma_{kk}/3$. Using eq. (5), the conservation of momentum is written in terms of the deviatoric stress and pressure:

$$\frac{\partial \tau_{ij}}{\partial x_j} - \frac{\partial p}{\partial x_i} = -\rho g_i \tag{6}$$

2.2. Constitutive equation of a visco-elastic fluid

The viscous constitutive law is conveniently expressed in terms of deviatoric stress τ_{ij} and deviatoric strain rate $\dot{\varepsilon}_{ij}$:

$$\tau_{ij} = 2\eta\dot{\varepsilon}_{ij} \tag{7}$$

where η is the shear viscosity, and the deviatoric strain rate tensor is defined as:

$$\dot{\varepsilon}_{ij} = \frac{1}{2}\left(\frac{\partial u_i}{\partial x_j} + \frac{\partial u_j}{\partial x_i}\right) - \frac{1}{3}\frac{\partial u_k}{\partial x_k}\delta_{ij} \tag{8}$$

Elastic deformation is incorporated by adopting a Maxwell material model, where the visco-elastic deviatoric strain rate is the sum of the viscous and elastic strain rates:

$$\dot{\varepsilon}_{ij} = \dot{\varepsilon}_{ij}^{visc} + \dot{\varepsilon}_{ij}^{el} = \frac{\tau_{ij}}{2\eta} + \frac{\breve{\tau}_{ij}}{2G} \tag{9}$$

where G is the shear modulus and $\breve{\tau}_{ij}$ is the objective deviatoric stress rate . The Zaremba-Jaumann objective time derivative (e.g. Hashiguchi and Yamakawa, 2012) is used to compute the objective deviatoric stress rate in eq. (9):

$$\breve{\tau}_{ij} = \frac{\partial \tau_{ij}}{\partial t} - \omega_{ik}\tau_{kj} + \tau_{ik}\omega_{kj} \tag{10}$$

where $\omega_{ij} = 1/2(\partial u_i/\partial x_j - \partial u_j/\partial x_i)$ is the spin tensor associated with the rigid body rotation. Following the implementation of large-strain elastic deformation described by Moresi et al. (2003) and Kaus (2010), $\breve{\tau}_{ij}$ is approximated by an implicit discretisation of the time derivative:

$$\breve{\tau}_{ij} \approx \frac{\tau_{ij}^{n+1} - \tau_{ij}^{n}}{\Delta t} - \omega_{ik}^{n}\tau_{kj}^{n} + \tau_{ik}^{n}\omega_{kj}^{n} \tag{11}$$

where the superscript n indicates the time step iteration, and Δt is the time step. Substitution of eq. (11) into eq. (9) with subsequent rearrangement of the terms leads to the visco-elastic constitutive law:

$$\tau_{ij} = 2\eta_{eff}\dot{\varepsilon}_{ij} + \chi\widehat{\tau}_{ij} \tag{12}$$

where

$$\eta_{eff} = \frac{1}{\frac{1}{\eta} + \frac{1}{G\Delta t}} \tag{13}$$

$$\chi = \frac{1}{1 + \frac{G\Delta t}{\eta}} \tag{14}$$

$$\widehat{\tau}_{ij} = \tau_{ij}^{n} + (\omega_{ik}^{n}\tau_{kj}^{n} - \tau_{ik}^{n}\omega_{kj}^{n})\Delta t \tag{15}$$

were the “real” viscosity has been substituted with an effective viscosity η_{eff} that includes elastic terms. A pure viscous rheology is recovered as $\Delta t \to \infty$. Note that the visco-elastic deformation obtained per time step depends on the size of the time step. However, the deformation after a certain simulation time has to be independent of the chosen time step.

2.3. Viscous creep

Two mechanisms for viscous deformation are included in the current treatment: diffusion creep and dislocation creep (Poirier, 1985; Karato et al., 2001). Diffusion creep occurs at low stress levels, when atoms diffuse inside the crystal grains and along the grain boundaries, resulting in rock deformation. Deformation due to dislocation creep is caused by the migration of dislocations through the crystal lattice of the rock. These creep mechanisms depend on temperature, pressure, and, for dislocation creep, strain rate:

$$\eta_{dif} = \frac{1}{2}(A_{dif}) \exp\left(\frac{E_{dif} + pV_{dif}}{nRT}\right) \tag{16}$$

$$\eta_{dis} = \frac{1}{2}(A_{dis})^{-\frac{1}{n_{dis}}} (\dot{\varepsilon}_{II}^{dis})^{\frac{1}{n_{dis}}-1} \exp\left(\frac{E_{dis} + pV_{dis}}{nRT}\right) \tag{17}$$

where A is the pre-exponential parameter, n is the power-law exponent (with, theoretically, $n \approx 3$ (Turcotte and Schubert, 2014)), $\dot{\varepsilon}_{II} = \sqrt{(1/2)\dot{\varepsilon}_{ij}\dot{\varepsilon}_{ij}}$ is the square root of the second invariant of the deviatoric strain rate tensor, E is the activation energy, V is the activation volume, R is the universal gas constant, and the sub-scripts dif and dis stand for diffusion and dislocation, respectively. We now build an effective creep viscosity as the harmonic mean of the diffusion and dislocation viscosities:

$$\frac{1}{\eta} = \frac{1}{\eta_{dif}} + \frac{1}{\eta_{dis}} \tag{18}$$

Here, the smallest viscosity has the largest contribution to the effective viscosity, with deformation dominated by the mechanism that has the smallest activation stress. The viscous strain tensor is then $\dot{\varepsilon}_{ij}^{visc} = \dot{\varepsilon}_{ij}^{dif} + \dot{\varepsilon}_{ij}^{dis}$. Using the definitions (16) and (17), the diffusion and dislocation strain tensors are respectively computed as:

$$\dot{\varepsilon}_{ij}^{dif} = \frac{\tau_{ij}}{2\eta_{dif}}; \quad \dot{\varepsilon}_{ij}^{dis} = \frac{\tau_{ij}}{2\eta_{dif}} \tag{19}$$

3. Numerical implementation

LaCoDe solves the resulting set of governing equations of the thermo-mechanical problem using the FEM to generate the system of matrix equations (e.g. Hughes, 1987; Zienkiewicz and Taylor, 2005). Discretising the domain into elements, the primary variables u, p and T are approximated using the shape functions N_u for velocity, N_p for pressure and N_T for temperature:

$$u(x, y) = \sum_{a=1}^{nu} N_u^a(x, y)\widetilde{u}_a \tag{20}$$

$$p(x,y) = \sum_{a=1}^{np} N_p^a(x,y)\widetilde{p}_a \tag{21}$$

$$T(x,y) = \sum_{a=1}^{nT} N_T^a(x,y)\widetilde{T}_a \tag{22}$$

where the subscript a is the nodal index and nu, np and nT is the number of nodes in the element for the velocity, pressure and temperature spaces. Employing the Galerkin procedure, the governing eqs. (1), (2) and (3) are transformed into their weak forms using the shape functions as trial functions.

The choice of the approximation space for the coupled velocity-pressure problem has to be taken carefully so that the so-called Ladyzhenskaya-Babuška-Brezzi (LBB) stability condition is satisfied (Zienkiewicz and Taylor, 2005). Some combinations of approximation spaces for velocity and pressure will violate such condition and result in spurious pressure modes and/or non-converged flow solutions. The LBB condition is satisfied in LaCoDe by using Crouzeix-Raviart triangular elements (Crouzeix and Raviart, 1973), where the velocity field is approximated by seven nodal points that define a quadratic interpolation enhanced by a cubic bubble function in the barycenter of the element (Fig .1). Pressure is discontinuous with three nodal points describing a linear interpolation within each element. Finally, temperature is approximated by six nodal points defining a quadratic interpolation.

[Figure 1 about here.]

In the following sections we detail the weak forms of the Stokes and thermal diffusion equations as well as their numerical implementation, where we drop the $\widetilde{\cdot}$ from the approximated fields in order to simplify the notation. The reader is referred to FEM textbooks (e.g. Hughes, 1987; Zienkiewicz and Taylor, 2005) for more details on this method, and how to build the weak formulation of the Stokes and thermal diffusion equations.

3.1. FEM formulation of thermal diffusion

The time derivatives in eq. (3) are approximated using a backward Euler discretisation:

$$\rho C_p \left(\frac{T^{n+1} - T^n}{\Delta t} \right) = \frac{\partial}{\partial x_i} \left(k \frac{\partial T^{n+1}}{\partial x_i} \right) + \alpha T^{n+1} \frac{p^{n+1} - p^n}{\Delta t} + H_r + H_{sh} \quad (23)$$

Using FEM for the spatial discretisation in space and rearranging eq. (23), we can express it in a compact matrix notation:

$$\mathbf{K}_T \mathbf{T} = \mathbf{f}_T \quad (24)$$

where the stiffness matrix is:

$$\begin{aligned} \mathbf{K}_T = \int_\Omega \nabla \mathbf{N}_T k \nabla \mathbf{N}_T d\Omega + \frac{1}{\Delta t} \int_\Omega \mathbf{N}_T^T \rho^{n+1} C_p \mathbf{N}_T d\Omega + \\ \frac{1}{\Delta t} \int_\Omega \mathbf{N}_T^T \alpha \mathbf{N}_u (\mathbf{p}^{n+1} - \mathbf{p}^n) \mathbf{N}_T d\Omega \end{aligned} \quad (25)$$

and the right-hand-side vector is:

$$\mathbf{f}_T = \frac{1}{\Delta t} \int_\Omega \mathbf{N}_T^T \rho^{n+1} C_p T^n \mathbf{N}_T d\Omega + \int_\Omega \mathbf{N}_T H_r d\Omega + \int_\Omega \mathbf{N}_T H_{sh} d\Omega \quad (26)$$

3.2. FEM formulation of Stokes equations

Motion of a compressible visco-elastic flow is described by the Stokes equations (1) and (2). The density time derivative in the continuity equation is computed in an implicit manner, so that eq. (2) is approximated as:

$$\frac{\partial u_i^{n+1}}{\partial x_i} = \frac{1}{\rho^{n+1}} \left(q_m - \frac{\rho^{n+1} - \rho^n}{\Delta t} \right) \quad (27)$$

The time derivative of density introduces a non-linearity in the system of equations, and eq. (2) can also be solved in an explicit manner. A comparison between both approaches is discussed in Heister et al. (2017) and, a priori, it is not obvious whether one approach is numerically more stable and/or more efficient than the other. By definition, the explicit approach would require fewer non-linear iterations than the implicit approach; however, Heister et al. (2017)

concluded that both approaches yield equally accurate results for similar computational time requirements. Employing the expression (27) for the continuity, the weak form of Stokes equations can be expressed in matrix form as:

$$\int_{\Omega} \mathbf{B}^T \mathbf{D} \mathbf{B} \mathbf{u}^{n+1} d\Omega - \int_{\Omega} \mathbf{B}^T \mathbf{m} \mathbf{N}_p \mathbf{p}^{n+1} d\Omega = \int_{\Omega} \mathbf{N}_u^T \rho \mathbf{g} d\Omega - \int_{\Omega} \mathbf{B}^T \chi \widehat{\tau} d\Omega \quad (28)$$

$$\int_{\Omega} \mathbf{N}_p^T \mathbf{m}^T \mathbf{B} \mathbf{u}^{n+1} d\Omega = \int_{\Omega} \mathbf{N}_P^T \left(\frac{1}{\rho^{n+1}} \left(q_m - \frac{\rho^{n+1} - \rho^n}{\Delta t} \right) \right) d\Omega \quad (29)$$

The element matrix $\mathbf{B}^e$ represents the strain-displacement matrix, while $\mathbf{D}^e$ is the rheology matrix that relates strain rates to deviatoric stresses:

$$\mathbf{B}^e \mathbf{u}^e = \begin{bmatrix} \frac{\partial N_u}{\partial x} & 0 \\ 0 & \frac{\partial N_u}{\partial z} \\ \frac{\partial N_u}{\partial z} & \frac{\partial N_u}{\partial x} \end{bmatrix} \begin{bmatrix} u_x \\ u_z \end{bmatrix} = \begin{bmatrix} \dot{\varepsilon}_{xx} \\ \dot{\varepsilon}_{zz} \\ \dot{\varepsilon}_{xz} \end{bmatrix} \quad (30)$$

$$\mathbf{D}^e = \eta_{eff} \begin{bmatrix} C_1 & C_2 & 0 \\ C_2 & C_1 & 0 \\ 0 & 0 & 1 \end{bmatrix} \quad (31)$$

$$\mathbf{m}^T = [1 \quad 1 \quad 0] \quad (32)$$

The $\mathbf{m}^T$ vector is necessary in the matrix form of these equations so that the cross derivatives in the last row of matrix $\mathbf{B}$ do not appear in some terms. For isotropic, compressible viscous flow, the coefficients in the rheology matrix $\mathbf{D}^e$ take values of $C_1 = 4/3$ and $C_2 = -2/3$ (e.g. Dabrowski et al., 2008). The weak forms (28) and (29) can then be written in a compact matrix notation as:

$$\begin{bmatrix} \mathbf{A} & \mathbf{G} \\ \mathbf{G}^T & \mathbf{0} \end{bmatrix} \cdot \begin{pmatrix} \mathbf{u} \\ \mathbf{p} \end{pmatrix} = \begin{pmatrix} \mathbf{f}_1 \\ \mathbf{f}_2 \end{pmatrix} \quad (33)$$

where:

$$\mathbf{A} = \int_\Omega \mathbf{B}^T \mathbf{D} \mathbf{B} d\Omega \tag{34}$$

$$\mathbf{G} = -\int_\Omega \mathbf{B}^T \mathbf{m} \mathbf{N}_p d\Omega \tag{35}$$

$$\mathbf{f}_1 = \int_\Omega \mathbf{N}_u^T \rho \mathbf{g} d\Omega - \int_\Omega \mathbf{B}^T \chi \widehat{\tau} d\Omega \tag{36}$$

$$\mathbf{f}_2 = \int_\Omega \mathbf{N}_P^T \left[\frac{1}{\rho^{n+1}} \left(q_m - \frac{\rho^{n+1} - \rho^n}{\Delta t} \right) \right] d\Omega \tag{37}$$

Note that the right-hand-side vector $\mathbf{f}_2$ contains the non-zero divergence terms related to density changes.

3.3. Solution scheme for the compressible Stokes equations

The system of eqs. (33) mathematically describes a so-called *saddle point* problem. Numerical complications arise due to the presence of the diagonal (2,2)-block in the matrix on the left-hand-side, which makes the matrix positive-semidefinite, so that it cannot be solved using standard forms of numerical algorithms such as Conjugate Gradient or Cholesky factorization that assume a symmetric positive-definite matrix. LaCoDe solves the Stokes equation using the Augmented Lagrangian method (Rockafellar, 1974; Fortin and Glowinski, 2000; Zienkiewicz and Taylor, 2005), which consists of subtracting $\lambda^{-1}\mathbf{M}\mathbf{p}$ from the left- and right-hand-side of the continuity equation, thereby generating the following iterative scheme:

$$\begin{bmatrix} \mathbf{A} & \mathbf{G} \\ \mathbf{G}^T & -\lambda^{-1}\mathbf{M} \end{bmatrix} \cdot \begin{pmatrix} \mathbf{u} \\ \mathbf{p} \end{pmatrix}^{k+1} = \begin{pmatrix} \mathbf{f}_1 \\ \mathbf{f}_2 - \lambda^{-1}\mathbf{M}\mathbf{p}^k \end{pmatrix} \tag{38}$$

where k is the iteration counter, λ is an artificial compressibility term penalising the new pressure term in the second row of the global block matrix that has units of dynamic viscosity, and $\mathbf{M}$ is the mass matrix defined as:

$$\mathbf{M} = \int_\Omega \mathbf{N}_p^T \mathbf{N}_p d\Omega \tag{39}$$

The choice of λ is not trivial, as the global block matrix problem may become ill-posed or numerical locking might occur if λ is too high or too low, respectively. A value of $\lambda = max(\eta)$ has been proven to work well in the following benchmarks. Upon convergence, $||\mathbf{p}^{k+1} - \mathbf{p}^k|| <$ tolerance and the system of eqs. (33) is recovered. The new system of eqs. (38) allows the elimination of the pressure field, so that the first and second rows of the system can be solved in a segregated manner. Rearranging the second equation we obtain the expression for the updated pressure:

$$\mathbf{p}^{k+1} = \mathbf{p}^k + \mathbf{M}^{-1}(\lambda \mathbf{G}^T \mathbf{u}^{k+1} - \mathbf{f}_2) \tag{40}$$

After substitution of eq. (40) into the first equation in the system (38) we obtain the following linearised expression for the velocity field:

$$\mathbf{u}^{k+1} = \mathbf{K}^{-1}\mathbf{f}^{k+1} \tag{41}$$

where the stiffness matrix $\mathbf{K}$ is defined as:

$$\mathbf{K} = \left(\mathbf{A} + \mathbf{G}\lambda\mathbf{M}^{-1}\mathbf{G}^T\right) \tag{42}$$

and the force vector in the right-hand-side is:

$$\mathbf{f}^{k+1} = \mathbf{f}_1 + \mathbf{G}\left(\lambda\mathbf{M}^{-1}\mathbf{f}_2 - \mathbf{p}^k\right) \tag{43}$$

The expression (40) is clearly non-linear because the density in $\mathbf{f}_2$ depends on the pressure via the equation of state (see eq.(4)). We treat this non-linearity by introducing a set of Picard iterations that freezes the density during the Augmented Lagrangian iterations:

$$\begin{aligned} \overbrace{\nabla \cdot \mathbf{u}^{k+1} + \frac{1}{\lambda}\mathbf{p}^{k+1}}^{\text{new velocity and pressure}} &= \underbrace{\frac{1}{\rho(\mathbf{P}^m, \mathbf{T}^m)}}_{\text{previous Picard iteration}} \cdot \\ \left(q_m - \frac{\overbrace{\rho(\mathbf{P}^m, \mathbf{T}^m)}^{\text{previous Picard iteration}} - \overbrace{\rho(\mathbf{P}^n, \mathbf{T}^n)}^{\text{previous time step}}}{\Delta t}\right) &= \mathbf{f}_2^m \end{aligned} \tag{44}$$

where the superscripts k, m and n are the counters of the Augmented Lagrangian, Picard and time iterations, respectively. Eqs. (40) and (41) are thus solved iteratively combining Augmented Lagrangian and Picard iterations in the following scheme (Fig .2):

1. $\mathbf{p}^0 = 0$ for $n = 1$, and $\mathbf{p}^0 = \mathbf{p}^{n-1}$ for $n > 1$.
2. Calculate: $\mathbf{K}$.
3. Calculate: $\mathbf{f}_2^m$
4. Calculate: $\mathbf{f}^{k+1}$
5. Solve: $\mathbf{u}^{k+1} = \mathbf{K}^{-1}\mathbf{f}^{k+1}$
6. Update pressure: $\mathbf{p}^{k+1} = \mathbf{p}^k + \mathbf{M}^{-1}(\lambda \mathbf{G}^T \mathbf{u}^{k+1} - \mathbf{f}_2^m)$
7. Check convergence of the continuity equation. If $\| -\mathbf{Q}^T\mathbf{u}^{k+1} - \mathbf{f}_2^n \|_\infty / \| -\mathbf{Q}^T\mathbf{u}^k - \mathbf{f}_2^n \|_\infty > \text{tol}_p$, repeat steps 4 and 6.
8. Check convergence of non-linearities in the continuity equation. $\| \mathbf{f}_2^m - \mathbf{f}_2^{m+1} \|_\infty > \text{tol}_{f2}$, repeat steps 3 to 7.

where $\| \cdot \|_\infty$ is the infinity norm, and $\text{tol}_p = 10^{-2}$, $\text{tol}_{f2} = 10^{-8}$. We note that for $\mathbf{p}^0 = 0$, the equations are equivalent to the penalty method. The solution scheme presented here is equivalent to the schemes resulting from Uzawa iterations (Arrow et al., 1958; Zienkiewicz, 1985) and later extended in the context of optimization independently by Hesteness (Hestenes, 1969) and Powell (Powell, 1967).

[Figure 2 about here.]

Alternatively, the system of eqs.(33) could be approximated using the Schur complement of the Stokes equations. However, the Schur complement $\mathbf{S} = \mathbf{G}\mathbf{A}^{-1}\mathbf{G}^T$ requires the computation of the inverse of the matrix $\mathbf{A}$ for a direct solution method, which is practically unobtainable, because it would be a very large and block matrix. In an iterative solver, this issue can be bypassed by the combination of the Schur complement with Conjugate Gradients or GMRES (e.g. Maday and Patera, 1989; Bangerth et al., 2011). For 2D calculations, the Augmented Lagrangian Method offers a simpler and computationally less expensive scheme to approximate the solution of the Stokes equations, because the discontinuous nature of the pressure field with Crouzeix-Raviart elements allows the inversion of $\mathbf{M}$ in eqs. (40) and (42) to be done on the element level. However, Crouzeix-Raviart elements do not have a three-dimensional equivalent and even the construction of a direct inverse for **A** becomes costly and memory intensive in 3D, hence the use of the Schur complement becomes more appropriate for 3D computations (e.g. Hasenclever (2010)).

3.4. Iteration scheme for non-linear rheology

The problem described in Section 3.3 becomes even more non-linear if temperature and/or a non-Newtonian rheology are also considered. We propose two different approaches to tackle highly non-linear problems (Fig .2): i) all the non-linearities are treated within a single loop of Picard iterations, referred as *Approach 1*; and, ii) the rheological and density non-linearities are split into two levels of nested Picard iterations, referred as *Approach 2*. While Approach 2 is likely to increase the total number of linear and non-linear iterations for a single time step, the rheological non-linearities are performed in a presumably better converged flow solution since the density non-linearities are first dealt with. The rheology iterations are stopped when the residual of the velocity field R is below a given tolerance:

$$R = \frac{\| u^{i+1} - u^{i} \|_{\infty}}{\| u^{i+1} \|_{\infty}} < \mathrm{tol}_u \tag{45}$$

where i is the rheology iteration counter, and a value for $\mathrm{tol}_u = 10^{-3}$. We note that this iterative scheme is able to handle other types of rheological non-linearities that are not discussed in this paper, such as plastic deformation. The efficiency of both approaches is compared in Section 5.2.

4. Remeshing

One of the drawbacks of using a Lagrangian formulation is that large deformation of the mesh usually leads to highly distorted elements. This issue is overcome by mapping the necessary variable fields onto a newly generated high quality mesh. One could perform a remeshing after every time step, but to reduce the associated computational cost and interpolation errors, a new mesh is generated only when the quality of the mesh falls below a given threshold.

Let us define a triangle with the area A, vertices a, b and c, and the smallest and largest angles α and β, respectively. We define the quality factor of the triangle to be:

$$q_n = \frac{4\sqrt{3}A}{\| ab \|^2 + \| ac \|^2 + \| bc \|^2} \tag{46}$$

where q_n is a measurement of equilaterality of the triangular element (i.e. $q_n = 1$ for an equilateral triangle). The remeshing algorithm is called only when a triangular element has $q_n < Tol_q$, $\alpha < Tol_\alpha$ or $\beta > Tol_\beta$. Unless specified, we use values of $Tol_{q_n} = 0.25$, $Tol_\alpha = 7°$ and $Tol_\beta = 170°$.

Fields that are computed at the nodes (e.g. temperature) are linearly interpolated onto the new nodal positions. The information from other fields associated with the elements (i.e. stress, density) is stored at the integration points of the elements, and is mapped onto the new mesh employing the following procedure:

1. Find the element of the old mesh containing the new integration point using the quick search algorithm *tsearch2* (*Mutils* package: http://milamin.sourceforge.net/downloads).
2. Calculate local coordinates of the new integration point with respect to the element in the old mesh.
3. The field $\Psi(x, y)$ is mapped element-to-element onto the old nodes using linear shape functions:

$$\Psi_a(x, y) = (N^a(\xi, \eta))^{-1}\Psi(x', y') \tag{47}$$

   where a is the nodal index, ξ and η are the local coordinates of the shape function and x' and y' are the coordinates of the integration point of the old mesh.
4. The nodal values of target field $\Psi_a(x, y)$ are mapped onto the new integration point using the shape functions:

$$\Psi(x^*, y^*) = \sum_{a=1}^{n} N^a(\xi, \eta)\Psi_a(x, y) \tag{48}$$

   where ξ and η are the local coordinates of the shape function and x^* and y^* are the coordinates of the integration point of the new mesh.

While this scheme works particularly well for perfect body-fitting meshes, in which case each element of the new and old meshes belongs to a single material type, other approaches may be better suited for non-body-fitting meshes. The accuracy of the remeshing scheme is demonstrated in Section 5.1.5.

[Figure 3 about here.]

5. Numerical experiments

We present a set of benchmarks and numerical experiments to test the implementation of the formulation described above. We first demonstrate the accuracy of LaCoDe by comparing the results of these experiments with analytical solutions and results from previously published studies. These benchmarks are: i) bending of a thin beam under a distributed load (Turcotte and Schubert, 2014); ii) SolCx (Zhong, 1996) and iii) SolKz tests (Revenaugh and Parsons, 1987); iv) deformation around a viscous inclusion (Schmid and Podladchikov, 2003); v) Rayleigh-Taylor instability (van Keken et al., 1997); vi) stress build-up in a visco-elastic Maxwell body (Gerya and Yuen, 2007); and vii) solution of a Couette-flow with viscous heating and temperature-dependent viscosity (Turcotte and Schubert, 2014). Then, we investigate the effectiveness of the two approaches to solve problems with non-linear rheologies described in Section 3.4. Finally, two tectonic scenarios where the effect of compressibility effects is relevant are presented: i) an example of volumetric strain produced by phase changes; ii) subduction of a compressible slab.

5.1. Benchmarks

5.1.1. Cantilever beam under a uniform load

In this benchmark we compare the numerical results of a bending elastic thin plate, clamped at one end, against an analytical solution for a perfectly-elastic material (Turcotte and Schubert, 2014). We also use this benchmark to compare the accuracy of the non-linearised and linearised formulations in resolving elastic problems. The ratio between the thickness and length of the cantilever is taken to be 1/10 in order to satisfy the thin beam hypothesis. The density of the beam is $\rho = 100\ kg/m^3$ (an approximate value for the density contrast between the upper and lower crust), and the shear modulus is $G = 36$ GPa. The analytical solution for the maximum deflection ω is

$$\omega = \frac{3}{24}\frac{\rho g h L^4}{D} \tag{49}$$

where h and L are the height and length, respectively, and D is the so-called flexural rigidity of the plate. The latter can be expressed in terms of the Young modulus E and the Poisson ratio ν: $D = Eh^3/12(1-\nu^2)$. The maximum horizontal stress in the cantilever is given by:

$$\sigma_{xx}^{max} = \frac{3\rho g L^2}{h^2} \tag{50}$$

[Figure 4 about here.]

To test the mesh-dependence and the accuracy of our code we use uniform meshes with different configurations of triangular elements. These meshes are constructed by splitting squares into two right triangles or four isosceles triangles, see Fig .4a. The deformed beam and the resulting stress field of the beam with $\nu = 0.25$ are shown in Fig .4b. The maximum deflection of the cantilever (Fig .4c) is accurately resolved for different degrees of elastic compressibility ($0.25 \leq \nu \leq 0.4999$). An excellent match to the analytical solution is achieved with only 8 elements in the vertical direction with relative errors $e_\omega < 1\%$ for all the Poisson ratios. Maximum horizontal stresses show high relative errors for coarse meshes but rapidly converge to the analytical solution with $e_{\sigma_{xx}} < 5\%$ for meshes with 8 elements in the vertical direction. Good accuracy of the solver is demonstrated in both the compressible and incompressible limits. Relative errors for $\nu < 0.45$ are consistent with the results obtained employing quadrilateral elements with 4 nodes by Popov and Sobolev (2008) and 8 nodes by Quinteros et al. (2009).

5.1.2. SolCx

This benchmark is intended to test the accuracy of the solution in the presence of large sharp jumps in the viscous field. The domain is $\Omega = [0, 1] \times [0, 1]$, the displacement in the corners is zero, and all the boundaries have null tangential stress (i.e. free slip). The flow inside the domain is driven by the buoyancy forces defined by the density field $\rho = sin(\pi y)cos(\pi x)$ and the viscosity field is defined by the piecewise function:

$$\eta(x, y) = \begin{cases} 1, & \text{if } 0 \leq x \leq 0.5 \\ 10^6, & \text{if } 0.5 < x \leq 1 \end{cases} \tag{51}$$

This strong viscosity jump yields a discontinuity in the pressure field between the two viscous domains, resulting in an excellent numerical experiment to assess the accuracy of the solver. The analytical solution of the flow and pressure fields is detailed in Zhong (1996). We consider an even and odd regular meshes of Crouzeix-Raviart elements constructed by splitting squares into two triangles rectangles. The number of nodes in the horizontal and vertical directions of the domain is $h^{even} = [8, 16, 32, 64, 128, 256]$ and $h^{odd} = h^{even} - 1$. The accuracy of the velocity and pressure fields is measured by computing the L_1 and L_2 norms. For a scalar field Ξ, the L_1 and L_2 norms are, respectively:

$$\| \Xi \|_1 = \int_V | \Xi | \, dV \tag{52}$$

$$\| \Xi \|_2 = \int_V \Xi^2 dV \tag{53}$$

And for a vector field v, the L_1 and L_2 norms are, respectively:

$$\| v \|_1 = \int_V (| v_1 | + | v_2 |) dV \tag{54}$$

$$\| v \|_2 = \int_V (v_1^2 + v_2^2) dV \tag{55}$$

The velocity and pressure errors converge with $\mathcal{O}(h^3)$ and $\mathcal{O}(h^2)$, respectively, both for the L_1 and L_2 norms, as well as in both even and odd meshes (Fig.5a). These orders of accuracy are comparable to the ones reported by Kronbichler et al. (2012) and Thielmann et al. (2014) employing even meshes of

$Q_2^d \times P_{-1}$ elements, and one order of accuracy greater than the errors report in Duretz et al. (2011). We must remark that even though the errors are a bit larger than in even meshes, the order of accuracy is the same for odd meshes of Crouzeix-Raviart, whereas $Q_2^d \times P_{-1}$ elements lead to lower convergence rates in odd meshes (Kronbichler et al., 2012; Thielmann et al., 2014).

5.1.3. SolKz

The so-called SolKz (Revenaugh and Parsons, 1987) test assesses the accuracy of the solver against large, smooth viscosity variations. The geometry of the domain, spatial discretisation, mesh resolution, and boundary conditions are identical as in the SolCx benchmark. However, only even meshes are tested due to the lack an internal layer. The flow inside the domain is driven by the buoyancy forces defined by the density field $\rho = sin(2y)cos(3\pi x)$, and the viscosity field smoothly increases from bottom to top:

$$\eta(y) = exp(2By) \tag{56}$$

where $B = \log_{10}(10^6)/2$, so that the viscosity contrast is of six orders of magnitude. As in the SolCx problem, velocity and pressure errors are measured in the L_1 and L_2 norms (Fig.5b).

[Figure 5 about here.]

The convergence rates obtained for this particular test are the same as for the SolCx test ((Fig.5, dashed lines)), and these errors are again comparable to the ones reported in Duretz et al. (2011), Kronbichler et al. (2012) and Thielmann et al. (2014).

5.1.4. Viscous inclusion

The set-up of this benchmark consists of a circular inclusion with radius $R = 0.1$ embedded in a homogeneous matrix under pure shear boundary conditions in a square domain $\Omega = [-1, 1] \times [-1, 1]$ (Fig.6a). As the SolCx test (Section 5.1.2), the aim of this experiment is to assess the accuracy of the pressure and velocity fields in cases with strong viscosity jumps. The dimensionless viscosity of the inclusion is $\eta_1 = 10^3$, and the viscosity of the matrix is $\eta_2 = 1$. The domain is discretised using an unstructured mesh of triangular elements that near-perfectly matches the matrix-inclusion interface. In other words, the edges of the elements match with the interface between the inclusion and the matrix, resulting in elements belonging either to one phase or the other. It has been shown that this type of spatial discretisation yields the most accurate solutions for this numerical experiment (Deubelbeiss and Kaus, 2008). For this particular test, the unstructured triangular mesh is generated with the mesh generator Triangle (Shewchuk, 1996). Velocity boundary conditions calculated from the analytical solution described in Schmid and Podladchikov (2003), using a background strain rate of $\dot{\varepsilon}_b = 1$, are prescribed on the boundaries of the model (see Appendix B). The pressure and velocity errors are calculated computed using the root-mean-square (rms) error so that our results can be compared with previous studies (e.g. Deubelbeiss and Kaus, 2008; Duretz et al., 2011; von Tscharner and Schmalholz, 2015):

$$rms = \sqrt{\frac{\int_\Omega (\chi^{num} - \chi^{ana})^2 d\Omega}{\int_\Omega (\chi^{ana})^2 d\Omega}} \tag{57}$$

where χ is the computed field, and the superscripts *num* and *ana* indicate the numerical and analytical values, respectively.

Both pressure and velocity show a monotonous convergence rate of first order with respect the number of degrees of freedom (DoFs), Fig .6b. Figs.6c-d show the pressure and velocity along the horizontal plane $y = 0$ for different numerical resolutions. Coarse meshes with low number of DoFs show accurate pressure solutions in the background matrix, whereas there is an evident drop in the accuracy of the numerical solution near the inclusion. Nevertheless, smoother pressure solutions around the inclusion are obtained with high spatial resolutions (DOF $> 10^4$). The velocity along the same plane displays higher levels of accuracy, with a smooth solution around the viscosity jump even for low numerical resolutions.

[Figure 6 about here.]

The analytical and numerical solutions for pressure and velocity are shown in Fig .7, as well as the distribution of the pressure and velocity error fields. As discussed above, the highest pressure errors are located around the interface between the inclusion and the matrix, while velocity errors are smoothly distributed over the matrix, with the minimum errors occurring inside the inclusion. The errors obtained with LaCoDe are comparable with other available repetitions of this test (e.g. Deubelbeiss and Kaus, 2008; Duretz et al., 2011; von Tscharner and Schmalholz, 2015).

[Figure 7 about here.]

5.1.5. Rayleigh-Taylor instability

The purpose of this test is to benchmark viscous deformation due to convection driven by density contrasts. This benchmark was designed by van Keken et al. (1997) and has been repeated several times by the geodynamics community (e.g. Bourgouin et al., 2006; Popov and Sobolev, 2008; Quinteros et al., 2009; Fuchs and Schmeling, 2013; Choi et al., 2013). The large deformation produced in this experiment provides an excellent way to validate not only the viscous deformation, but also the implementation of the remeshing algorithm. Both fluids are assumed to be isoviscous with equal viscosity but different density. In this test we use the dimensionless equation of conservation of momentum:

$$\frac{\partial \tau_{ij}}{\partial x_j} + \frac{\partial P}{\partial x_j} = R_b \Gamma n_j \tag{58}$$

[Figure 8 about here.]

where n_j is the unit vector in the direction j and $R_b = \Delta\rho g h^3/\kappa\eta_r$ is the "compositional Rayleigh number" , where η_r is the reference viscosity. Γ is a step function with $\Gamma = 1$ for the layer at the bottom and $\Gamma = 0$ for the top layer. The domain consists of a box of height h and width λ. The thickness of the bottom layer is 0.2 with an initial perturbation between the two phases given by:

$$\omega = 0.02 \cos\left(\frac{\pi x}{\lambda}\right) \tag{59}$$

The aspect ratio of the domain ($\lambda = 0.9142$) is chosen such that a harmonic perturbation with wavelength 2λ is the most unstable, giving the largest growth rate. Displacements are restricted at the bottom and top boundaries and tangential free-slip is allowed along the lateral boundaries (Fig .8a).

We consider only an isoviscous case with $\rho_r/\rho_o = 1.3$. Throughout the evolution of the flow we calculate the evolution with time of the root-mean-square velocity (van Keken et al., 1997):

$$u_{rms}(t) = \sqrt{\frac{1}{h\lambda}\int_0^\lambda \int_0^h \parallel u \parallel^2 \, dxdz} \tag{60}$$

We use the 'best' results from van Keken et al. (1997) as a reference (Pvk code with 80x80 C1 finite elements) to validate the results obtained with LaCoDe. The Rayleigh-Taylor instability shows the same evolution (Fig .8a-e) as the one shown by van Keken et al. (1997), and only a few discrepancies are found in the geometry of the secondary and tertiary diapirs in the late stages of the flow evolution. Models with coarse meshes are able to predict accurate values of the maximum rms velocity, but predict maximum rms velocities for the secondary diapir that are 13% higher than the values obtained with a finer mesh (Fig .8f). The growth rate of the instability γ at the dimensionless time $t = 0$ and the maximum rms velocity (Table .1) are in agreement with the reference values, with errors smaller than 1%. The increase in the difference of the maximum u_{rms} for the case with 17960 elements is due to a numerical resolution 2.8 times higher than the one employed in the reference case, presumably leading to a more accurate solution.

[Table 1 about here.]

The remeshing algorithm is called when the quality of any element or elements of the mesh is below the quality threshold. The two fluids are spatially discretised such that their interface represents a sharp contact, with individual elements belonging to a single phase. This interface is tracked with time, and it is used to define the geometry of the new mesh. The interface between the two fluids undergoes a high amount of stretching during the evolution of the flow and must be refined when remeshing becomes necessary, so that the spatial resolution along this boundary is constant. This is done by adding a new node in the midpoint between two consecutive nodes if the distance between them is larger than a specified value. This procedure yields a considerable increase of the number of elements with respect to the initial mesh, as the model evolves with time. As for the viscous inclusion test, the unstructured triangular mesh is generated with Triangle (Shewchuk, 1996).

In this numerical experiment, it is sufficient to generate a new mesh and transfer the step function value, which is an element property. There is no actual need to transfer additional information from the old to the new mesh. However, for benchmarking purposes, we perform the mapping of the second invariant of the accumulated strain ε_{II}^{acc} onto the new high quality mesh. Fig .8g,h shows an accurate mapping of ε_{II}^{acc} from the old mesh onto the new mesh. The quality of the remeshing algorithm is assessed by comparing the finite strain field before and after remeshing. In order to compare the pre- and post-remeshing results, both fields are sampled in a high-resolution regular grid of 1000 by 1000 points, where the root-square error of the mapped field is computed (Fig .8i). The remeshing scheme yields a root-mean-square error on the order of 10^{-2}, with a standard deviation of 0.0569. Considering added errors due to the additional interpolation onto a regular grid for numerical comparison to the pre-remeshing field, remeshing errors are to be generally anticipated to be lower than in Fig .8i.

5.1.6. Stress build-up in a visco-elastic Maxwell body

Visco-elastic deformation is demonstrated by repeating the numerical experiment of stress build-up in a Maxwell body under pure shear deformation . A constant background strain rate $\dot{\varepsilon} = 10^{-15}\ s^{-1}$ is prescribed at the boundaries of a body of 100 by 100 km size (Fig .9a). The mechanical parameters are: $G = 10$ GPa, $\eta = 10^{22}$ Pa $\cdot$ s and gravity is switched off. We take $\nu = 0.4999$ in order to approximate an incompressible material. The build-up of the stress is described by the following analytical expression (Gerya and Yuen, 2007):

$$\tau_{II} = 2\dot{\varepsilon}_{II}(1 - exp(-\frac{Gt}{\eta})) \quad (61)$$

The analytical and numerical time-stress curves overlap (Fig .9b,c), demonstrating the high accuracy of the implementation of the Maxwell rheology.

[Figure 9 about here.]

5.1.7. Couette flow with viscous heating- and temperature-dependent viscosity

[Figure 10 about here.]

The aim of this test is to demonstrate the accuracy of the numerical solution of thermal diffusion and the coupling of the Stokes equations for fluids with temperature-dependent viscosity and shear heating. The set-up of the model is consists of the Couette flow in a rectangular channel (Fig.10a). The motion of the flow is driven by shear along the top boundary of the channel with the following boundary conditions: no displacement and $T = T_0$ at the lower boundary, constant shear stress and $\partial T/\partial x = 0$ at the lateral boundaries of the model. The size of the model is $\Omega = [0, 90] \times [0, 12]$ km. This aspect ratio is sufficiently large to avoid errors in the flow due to boundary effects. The model is started with T_0 across the whole domain.

The dependence of the maximum non-dimensional temperature change in the channel θ with the Brinkman number Br (a dimensionless number related to heat conduction from a wall to a flowing viscous fluid (Turcotte and Schubert, 2014)) is used to compare the analytical solution (Appendix D) against the numerical results. The results obtained with LaCoDe show an excellent agreement with the analytical solution (Fig.10), demonstrating the capability of the code to model coupled thermo-mechanical problems with non-linear rheologies and shear heating.

5.2. Non-linear rheology iterations: single vs. nested Picard iterations

We test the accuracy and efficiency of these two solution schemes with two different numerical experiments: A) a visco-elastic rectangular body under pure shear with a non-Newtonian rheology including diffusion and dislocation creep; and, B) a set-up for a subduction problem with a non-Newtonian visco-elastic rheology. In both problems, we keep track of and compare the number of linear and non-linear iterations, residual velocity and computational time during the first ten time steps for Test A, and six time steps for the Test B (this corresponds to the number of time steps before remeshing is required). Details of the model set-up, boundary conditions and thermo-mechanical parameters are found in Appendix C.

[Figure 11 about here.]

Results from Test A (Fig .11a) show that, as expected, Approach 2 leads to a higher number of Powell-Hestenes iterations compared to dealing with all non-linearities in the same loop as in Approach 1, resulting in typically $\sim 150\%$ times more linear iterations and $\sim 25\%$ additional computational time per iteration. Despite being somewhat more expensive, Approach 2 yields a better-converged solution.

The efficiency of Approach 1 and 2 is further checked with the more realistic Test B, where a rheologically layered domain adds new degrees of complexity to the problem. In this case we have capped the maximum number of the outer level of Picard iterations to 60. Approach 2 converges typically within 17-30 outer Picard iterations, whereas Approach 1 constantly reaches the maximum allowed number of iterations and results in a poorly-converged solution (Fig .11b). In this case, every time step using Approach 2 needs to perform about 2 or 3 times the number of linear iterations performed by Approach 1; however, approximately half of the rheological non-linear iterations are required, yielding a slightly cheaper solution scheme.

Considering these results, we infer that treating all the non-linearities in one level of Picard iterations (Approach 1) is more efficient in terms of total number of iterations; however, this approach yields larger residuals of the velocity field (Fig .11). Approach 2 also becomes substantially cheaper than Approach 1 as the complexity of the problem increases because a lower number of outer Picard iterations is required. We therefore recommend to use the solution scheme in Approach 2 for geometrically complex and highly non-linear problems.

5.3. Numerical experiments with a compressible lithosphere and asthenosphere

5.3.1. Volumetric strain induced by serpentinisation

The phase change from peridotite to serpentinite is accompanied by a considerable volume expansion and reduction in density. In this experiment, we simulate a visco-elastic oceanic lithosphere in which serpentinisation occurs to different degrees. The transformation of mantle peridotites to serpentinite occurs within a specific range of pressure and temperature and with an inflow of sea water into the material. However, in the model shown here, we simplify this process by imposing a rate of density change in a target region, at a rate that reaches the maximum degree of serpentinisation after 1 Myr. This experiment is designed to explore the impact of the rapid expansion and reduction in density on the stress and strain fields.

The model is 300 km long and 100 km deep and is stretched under pure shear boundary conditions, with a full extension rate of $u_{ext} = 1$ mm/yr. Serpentinisation occurs within the 40 km by 10 km rectangular area located at the centre of the model. The rheology is visco-elastic with $\eta = 10^{23}$ Pa s, $G = 36GPa$ and $\nu = 0.3$. A lithostatic approximation of the pressure is used to define the reference density. The density of the serpentinised material is calculated as a linear function of β (Escartin et al., 2001):

$$\rho(\beta) = \rho_{serp} \left(1 - \frac{\beta}{100}\right) (\rho_o - \rho_{serp}) \tag{62}$$

where β is the percent of serpentinisation. We take a $\rho_o = 3300$ kg/m^3 characteristic of mantle material, and $\rho_{serp} = 2550\ kg/m^3$. We run a set of models with different values of degree of serpentinisation ($\beta = 0$, 20 and 40%).

[Figure 12 about here.]

It is known that at these values of serpentinisation, significant weakening of the lithosphere should occur (Escartin et al., 1997; Maffione et al., 2015). Considering a pressure dependent failure criterion such as Drucker-Prager , $\tau_y = p\sin(\phi) + C\cos(\phi)$, and assuming cohesion $C = 20$ MPa and friction angle ϕ between 10° and 30° (dashed line in Fig.12b), it becomes evident that the stress linked to the volumetric increased caused by serpentinisation reactions can easily exceed the yield stress at shallow depths (at ~ 2 km for $\beta = 20\%$ and ~ 10 km for $\beta = 40\%$; Fig.12b), thus localising, or enhancing, inelastic deformation in faults and shear bands. Topographic expressions in the seafloor could also be linked to the production of serpentinite at shallow depths (Fig.12c). Our models predict topographic highs of 0.3 km and 0.7 km for a partially serpentinised material for $\beta = 20\%$ and $\beta = 40\%$, respectively.

For comparison, we include a model with $\beta = 40\%$ using the incompressible Boussinesq approximation (i.e. the continuity equation is approximated as $\nabla \cdot \mathbf{u} = 0$ and the

equation

of state is pressure-independent). The incompressible approximation is not able to resolve the volumetric strain and the flow solution only accounts for the buoyancy forces produced by the serpentinisation. Therefore, the strain field is barely affected by the phase change and the stress field is incorrect, showing even lower stresses than for $\beta = 0\%$ (Fig.12b). Furthermore, the pressure dependence of the density in this model is switched off as it would become unstable after few time steps.

Even though the model considered here is very simple, and more realistic set-ups and conditions might change the values of the effect of serpentinisation (e.g. plastic deformation, rheological layering, etc.), it serves as an example of how the volumetric strain produced by a phase change can potentially weaken the crust and localise brittle deformation. Therefore, weakening by serpentinisation may play a crucial role to shape the kinematics of magma-poor margins and the bending/unbending of subducting plates (Morgan, 2001). This thought numerical experiment also represent a case in which the incompressible Boussinesq approximation is not able to deal with large density changes and predicts unrealistic strain and stress fields. In such cases, a compressible formulation should be used.

5.3.2. Subduction of a compressible slab

[Figure 13 about here.]

In subduction zones, the cold subducting plate might sink to great depths, where it is subject to considerable pressure changes that should induce large variations in density. In this test, we investigate how large these density variations can be for a compressible mantle and lithosphere, and whether they eventually become large enough so that the Boussinesq approximation becomes inaccurate. The asthenospheric mantle and lithosphere are modeled as a non-Newtonian visco-elastic body. The mechanical parameters, set-up, and boundary conditions for subduction are described in Appendix C.2. Thermal ages of the oceanic and continental lithospheres are chosen as 70 Myr and 400 Myr, respectively. As in the previous example, the reference density is defined by an approximation of the lithostatic pressure. For completeness, the results obtained for a compressible ($\nu = 0.30$) asthenospheric mantle and lithosphere are compared with the near-incompressible case ($\nu = 0.499$). In the compressible case, ridge push (i.e. oceanic lithosphere pushed towards the continental lithosphere) is active until 4 Myr. At this moment, the tip of the slab is dense enough for slab-pull to become effective, and no additional forces are required to sustain the subduction of the oceanic lithosphere. The density in the near-incompressible case is lower, and ridge push is active until 6 Myr.

At 3.5 Myr, while ridge push is still active, the compressible oceanic lithosphere has subducted approximately 300 km, and the dip at its tip is 50° (Fig .13a). After slab-pull becomes effective, the trench starts to retreat and the slab rolls-back. At 8.3 Myr, the dip increases to 75° the pressure at the tip of the slab is high enough to produce density variations with respect to the reference state that exceed the accuracy threshold of the Boussinesq approximation (Fig

.13a). At this point the trench has retreated 125 km, the slab is 14° steeper, and has further subducted down to 475 km depth (Fig .13a).

On the other hand, at 3.5 Myr and with ridge push active, the near-incompressible oceanic lithosphere subducts down to 275 km depth, and the maximum dip of slab is 10° less with respect the compressible case. At 8.3 Myr, the differences between the compressible and near-incompressible case become more evident, with the subducting slab being 70 km shallower and 10° less steep than for $\nu = 0.30$.

It is also worth noting the difference of the total pressure between the compressible and near-incompressible case (isobars in Fig .13a). In the first case, strong pressure gradients are predicted within the slab, with pressure drops at the core of the slab, and an increase of the pressure at the top boundary of the slab, whereas pressure gradients are almost negligible in the near-incompressible case.

This simple numerical experiments illustrates how compressibility is a mechanical feature that is certainly important to account for in models of subducting slabs. The large pressures that build up within the slab can lead to density variations of more than 10% that can influence the timing and effectiveness of slab pull, and the dynamics of subduction.

6. Discussion and summary

1. LaCoDe is a robust numerical tool for thermo-mechanical geodynamic problems that includes a new self-consistent compressible formulation. As a sequential-only MATLAB-based algorithm, the lack of computational speed compared to other highly-parallelised codes written in lower-level languages such as C/C++/Fortran is compensated by MATLAB's easy-debugging-fast-coding environment that runs in any workstation, and does not build upon any other compliances (only an interaction with a mesh generator is needed to construct unstructured finite element meshes).
2. LaCoDe is easily expandable: implementation of new rheological laws or

processes such as partial melting other phase changes require minimum code modifications. Hence this code is an excellent ”numerical laboratory” where new features can be quickly implemented and tested.

3. An implicit approach of the general compressible Stokes equation leads to a well-resolved solution employing iterative solvers such as the Augmented Lagrangian Method.

4. The density-dependence of the compressible continuity equation introduces an additional non-linearity with respect to the incompressible approximation, thus increasing the total number of iterations per time step. We find that for non-Newtonian rheologies, one can treat all non-linearities within one Picard loop. However, as the complexity of the problem increases, it becomes convenient to split the non-linearities with a rheological nature from the ones raising from the continuity equation into two levels of Picard iterations, this leads to faster convergence rates and best resolved solutions. Preliminary experiments indicate that this remains true when plastic deformation is incorporated as an additional non-linear rheological complexity to the model treatment.

5. While the Boussinesq approximation is a valid hypothesis for simple modeling of crustal deformation, more complex models that aim to study processes such as phase changes or subduction of oceanic lithosphere will require a modification of the Boussinesq approximation to accommodate the chemical reaction- and pressure-linked effects of volumetric strain and volume-change-linked stresses.

6. Benchmarks for elastic deformation and stresses show that the formulation presented here is able to model elasticity both for compressible materials and in the incompressible limit.

7. Geodynamic models frequently require strong and sharp compositional jumps. We have demonstrated that the formulation implemented in LaCode is able to solve accurately the Stokes equations under strong (e.g. SolCx, viscous inclusion under pure shear) and smooth (e.g. SolKz test) viscosity, as well as in density contrasts leading to gravitational instabili-

ties (e.g. Rayleigh-Taylor instability).

8. The agreement of the numerical and analytical solution of a Couette flow with viscous heating and temperature dependent viscosity demonstrates the accuracy of LaCoDe to solve thermo-mechanical problems.
9. We demonstrate how compressibility may play an important role in some geodynamic processes that undergo strong pressure gradients, such as in subducting slabs, and when rapid density changes take place, such as during phase transformations. In the latter case, the presence of a self-consistent volume change source term is a powerful tool that opens an opportunity to study the effects of pressure changes caused by the inflow and outflow of mass into geological features (e.g. serpentinisation and melt extraction). Exploring these processes will be the aim of future work.

Acknowledgements

This study was supported by the SE Asia Research Group which is funded by a consortium of oil companies. We gratefully thank Cedric Thieulot and an anonymous for their thorough comments, that greatly improved the manuscript.

Appendix A. Analytical solution for a thin beam under uniform load

The general equation describing the deflection ω of an elastic cantilever of length L and thickness h is given by:

$$D\frac{d^4\omega}{dx^4} = q(x) - F\frac{d^2\omega}{dx^2} \tag{A.1}$$

where $q(x)$ is the load and F is the horizontal force. Considering $F = 0$ and a constant and uniform load, eq. (A.1) yields:

$$\frac{d^4\omega}{dx^4} = \frac{q}{D} \tag{A.2}$$

Eq. (A.2) can be integrated using the following boundary conditions: 1) $\omega = 0$ at $x = 0$ (fixed end); 2) $d\omega/dx = 0$ at $x = 0$; 3) $d\omega^2/dx^2 = 0$ at $x = L$; and,

4) $dM/dx = V$, where M is the bending momentum and V is the shear force. After some algebra, the solution can be written as:

$$\omega = \frac{qx^2}{D}\left(\frac{x^2}{24} + \frac{Lx}{6} + \frac{L^2}{4}\right) \tag{A.3}$$

with the q being the gravitational load $q = g\rho Lh$. The horizontal stress along the cantilever is given by the expression:

$$\sigma_{xx} = \frac{E}{1-\nu^2}\varepsilon_{xx} \tag{A.4}$$

the horizontal strain is given by:

$$\varepsilon_{xx} = -z\frac{d^2\omega}{dx^2} \tag{A.5}$$

and the bending momentum at $x = 0$ is:

$$M = -\frac{qL^2}{h} \tag{A.6}$$

The maximum bending stress at $x = 0$ in a cantilever, centred at $z = 0$, occurs at $z = \pm h/2$ and it is obtained combining eqs. (A.4), (A.5) and (A.6):

$$\sigma_{xx}^{max} = \frac{3qL^2}{h^2} \tag{A.7}$$

Appendix B. Analytical solution for a viscous inclusion

The analytical solution of a viscous inclusion within a homogeneous matrix is based on Muskhelishvili's complex variable stress-function method and solution (Muskhelishvili, 1953) for 2D elasticity. Here we present a brief description with the solution under pure shear conditions. A more detailed description in the geological literature is found in (Schmid and Podladchikov, 2003). The coordinates are expressed in the complex plane:

$$z = x + iy \tag{B.1}$$

where $i = \sqrt{-1}$. For a slow incompressible viscous flow in plane strain, the velocity field can be expressed in terms of the complex functions $\phi(z)$ and $\psi(z)$:

$$u_x + iu_z = \frac{\phi(z) - z\overline{\phi'(z)} - \overline{\psi(z)}}{2\eta} \tag{B.2}$$

where the overbar refers to the complex conjugate and the prime refers to the derivative with respect to z. Under pure shear boundary conditions the functions $\phi(z)$ and $\psi(z)$ in the matrix are given by:

$$\phi_m(z) = -\frac{2\dot{\varepsilon}Ar_c^2}{z} \tag{B.3}$$

$$\psi_m(z) = -2\dot{\varepsilon}\eta_m z - \frac{2\dot{\varepsilon}Ar_c^4}{z^3} \tag{B.4}$$

with

$$A = \frac{\eta_m\left(\eta_c - \eta_m\right)}{\eta_c + \eta_m} \tag{B.5}$$

where r_c is the radius of the inclusion and η_m and η_c are the viscosities of the matrix and the inclusion, respectively. Inside the inclusion:

$$\phi_c(z) = 0 \tag{B.6}$$

$$\psi_c(z) = -4\dot{\varepsilon}\frac{\eta_c\eta_m}{\eta_c + \eta_m}z \tag{B.7}$$

Substitution of eqs. (B.3) and (B.4) into (B.2) yields the analytical solution for the velocity field in the matrix:

$$u_x + iu_z = \frac{\dot{\varepsilon}Ar_c^2}{\eta_m}\left[-\frac{1}{z} + \frac{z}{\bar{z}^2} - \frac{1}{\bar{z}^3} - \frac{\bar{z}\eta_m}{Ar_c^2}\right] \tag{B.8}$$

Substitution of (B.6) and (B.7) into (B.2) gives the analytical solution for the velocity inside the inclusion:

$$u_x + iu_z = -\frac{4\dot{\varepsilon}}{2\eta_c}\frac{\eta_c\eta_m}{\eta_c + \eta_m}\bar{z} \tag{B.9}$$

The general expression of the pressure field is given by:

$$p = -2Re(\phi'(z)) \tag{B.10}$$

with $Re(\cdot)$ denoting the real part of $(\cdot)$. Under pure shear boundary conditions the pressure field in the inclusion is $p_c = 0$ and the pressure in the matrix is given by:

$$p_m = -2Re\left(\frac{2\dot{\varepsilon}Ar_c^2}{z^2}\right) \tag{B.11}$$

Appendix C. Model set-up and boundary conditions for tests in Section 3.4

Appendix C.1. Test A: Pure shear deformation of a non-Newtonian visco-elastic body

The initial size of the models is a 500 km by 400 km rectangular box with an initial temperature profile as shown in (Fig .14a). We use a non-Newtonian visco-elastic rheology with the thermo-mechanical parameters of wet olivine (Table .2). Pure shear far-field boundary conditions are prescribed on the boundaries of the model (i.e. half and full extension rate are prescribed at the lateral and bottom boundaries of the domain, respectively), the boundaries of the model are thermally insulated, tangential free slip condition are prescribed at the lateral and bottom boundaries and the surface behaves as a free surface. Temperature is fixed at 0 $^{\circ}C$ and 1300 $^{\circ}C$ at the surface and bottom of the model. The domain of the model is discretised with an unstructured mesh of 13828 triangular elements (42271 DoFs).

Appendix C.2. Test B: Subduction initiation

The set-up of Test B corresponds to a subduction problem in a box of 3000 km by 1500 km. Oceanic and continental lithosphere are 80 km and 140 km thick, respectively. The motion of the bottom and lateral sides is fixed, and convergence is imposed by prescribing a horizontal velocity along a vertical profile of the oceanic lithosphere 500 km before the trench. We use a non-Newtonian visco-elastic rheology with a wet quartzitic crust, dry olivine continental lithosphere and wet olivine for the oceanic lithosphere and asthenosphere. All side boundaries are thermally insulating; bottom and top temperatures are constant at 0 $^{\circ}C$ and 1300 $^{\circ}C$, respectively; and free surface boundary conditions are prescribed at the top of the model. The initial thermal structure is given by continental lithosphere with a thermal age of 500 Myr and an oceanic lithosphere with a thermal age of 75 Myr. To ease subduction initiation, we introduce a weak layer between the oceanic and continental lithospheres which has a constant viscosity of $5 \cdot 10^{19}$ Pa·s. The domain of the model is discretised by an unstructured mesh of 17927 triangular elements (55107 DoFs).

[Figure 14 about here.]

[Table 2 about here.]

Appendix D. Analytical solution for a Couette flow with viscous heating and temperature dependent viscosity

The non-Newtonian viscosity of the flow is controlled by the following equation (Turcotte and Schubert, 2014):

$$\eta = A \exp\left[\frac{E_a}{RT_0}\left(1 - \frac{T - T_0}{T_0}\right)\right] \tag{D.1}$$

where E_a is the activation energy, R is the gas constant and A is a pre-exponential factor that depends on the material. The analytical solution for the temperature field of the flow is described by the following set of equations (Turcotte and Schubert, 2014):

$$x = \frac{L}{B} ln\left[\frac{(D-B)(C-B)}{(D-B)(C+B)}\right] \tag{D.2}$$

$$B = ln\left[\frac{1 + \left(1 - \frac{2Br}{B^2}\right)^2}{1 + \left(1 + \frac{2Br}{B^2}\right)^2}\right] \tag{D.3}$$

$$C = \sqrt{2(\phi_1 - \phi(x))Br} \tag{D.4}$$

$$D = \sqrt{2(\phi_1 - 1)Br} \tag{D.5}$$

$$\phi(x) = exp(\theta(x)) \tag{D.6}$$

$$\theta(x) = \frac{E_a T(x) - T_0}{RT_0^2} \tag{D.7}$$

$$\phi_1 = \frac{B^2}{2Br} = exp(\theta_1) \tag{D.8}$$

$$\theta_1 = \frac{E_a(T_1 - T_0)}{RT_0^2} \tag{D.9}$$

$$Br = \frac{(\sigma_{xz1} L)^2 E_a}{KART_0^2} exp\left(-\frac{E_a}{RT_0}\right) \tag{D.10}$$

where Br is the non-dimensional Brinkman number, θ is the non-dimensional temperature change, σ_{xz1} is the shear stress at the top boundary, K is the thermal conductivity and T_1 is the temperature at the top boundary. If non-negative values of B are chosen, the Brinkman number can be calculated as (Gerya, 2009):

$$Br = \frac{B^2}{2}\left[1 - \left(\frac{exp(B) - 1}{exp(B) + 1}\right)\right] \tag{D.11}$$

For a given σ_{xz} the solution is non-unique and two flows with different temperature and velocity exist. However, a unique solution exists if a given velocity is prescribed at the upper boundary. Therefore, we prescribe a constant horizontal velocity boundary u^* at the upper boundary instead of imposing a constant shear stress. The input parameters for this test are $E_a = 150$ J/mol, $R = 8.35$, $A = 10^{15}$ Pa·s, $K = 2$ W/m/K and $T_0 = 1000$ K

References

Andrés-Martínez, M., Morgan, J. P., Pérez-Gussinyé, M., Rüpke, L., 2015. A new free-surface stabilization algorithm for geodynamical modelling: Theory and numerical tests. Physics of the Earth and Planetary Interiors 246, 41–51.

Arrow, K. J., Hurwicz, L., Uzawa, H., Chenery, H. B., 1958. Studies in linear and non-linear programming. Stanford University Press.

Bangerth, W., Burstedde, C., Heister, T., Kronbichler, M., 2011. Algorithms and data structures for massively parallel generic adaptive finite element codes. ACM Transactions on Mathematical Software (TOMS) 38 (2), 14.

Bercovici, D., Schubert, G., Glatzmaier, G. A., 1992. Three-dimensional convection of an infinite-prandtl-number compressible fluid in a basally heated spherical shell. Journal of Fluid Mechanics 239, 683–719.

Bourgouin, L., Mühlhaus, H.-B., Hale, A. J., Arsac, A., 2006. Towards realistic simulations of lava dome growth using the level set method. Acta Geotechnica 1 (4), 225–236.

Braun, J., Sambridge, M., 1994. Dynamical Lagrangian Remeshing (dlr): a new algorithm for solving large strain deformation problems and its application to fault-propagation folding. Earth and Planetary Science Letters 124 (1), 211–220.

Choi, E., Tan, E., Lavier, L., Calo, V. M., 2013. DynEarthSol2D: An efficient unstructured finite element method to study long-term tectonic deformation. Journal of Geophysical Research: Solid Earth 118 (5), 2429–2444.

Christensen, U. R., 1987. Some geodynamical effects of anisotropic viscosity. Geophysical Journal International 91 (3), 711–736.

Crouzeix, M., Raviart, P.-A., 1973. Conforming and nonconforming finite element methods for solving the stationary stokes equations i. Revue française d'automatique, informatique, recherche opérationnelle. Mathématique 7 (3), 33–75.

Dabrowski, M., Krotkiewski, M., , D. W., 2008. MILAMIN: MATLAB-based finite element method solver for large problems. Geochemistry, Geophysics, Geosystems 9 (4), 1–24.

Deubelbeiss, Y., Kaus, B., 2008. Comparison of Eulerian and Lagrangian numerical techniques for the stokes equations in the presence of strongly varying viscosity. Physics of the Earth and Planetary Interiors 171 (1), 92–111.

Duretz, T., May, D. A., Gerya, T., Tackley, P., 2011. Discretization errors and free surface stabilization in the finite difference and marker-in-cell method for applied geodynamics: A numerical study. Geochemistry, Geophysics, Geosystems 12 (7).

Escartin, J., Hirth, G., Evans, B., 1997. Effects of serpentinization on the lithospheric strength and the style of normal faulting at slow-spreading ridges. Earth and Planetary Science Letters 151 (3), 181–189.

Escartin, J., Hirth, G., Evans, B., 2001. Strength of slightly serpentinized peridotites: Implications for the tectonics of oceanic lithosphere. Geology 29 (11), 1023–1026.

Fortin, M., Glowinski, R., 2000. Augmented Lagrangian methods: applications to the numerical solution of boundary-value problems. Vol. 15. Elsevier.

Fuchs, L., Schmeling, H., 2013. A new numerical method to calculate inhomogeneous and time-dependent large deformation of two-dimensional geodynamic flows with application to diapirism. Geophysical Journal International 194 (2), 623–639.

Fullsack, P., 1995. An arbitrary Lagrangian-Eulerian formulation for creeping flows and its application in tectonic models. Geophysical Journal International 120 (1), 1–23.

Gerya, T., 2009. Introduction to numerical geodynamic modelling. Cambridge University Press.

Gerya, T. V., Yuen, D. A., 2007. Robust characteristics method for modelling multiphase visco-elasto-plastic thermo-mechanical problems. Physics of the Earth and Planetary Interiors 163 (1), 83–105.

Gleason, G. C., Tullis, J., 1995. A flow law for dislocation creep of quartz aggregates determined with the molten salt cell. Tectonophysics 247 (1), 1–23.

Gray, D. D., Giorgini, A., 1976. The validity of the Boussinesq approximation for liquids and gases. International Journal of Heat and Mass Transfer 19 (5), 545–551.

Hasenclever, J., 2010. Modeling mantle flow and melting processes at mid-ocean ridges and subduction zones. Development and application of numerical models. Ph.D. thesis, Hamburg University, Hamburg, Germany.

Hasenclever, J., Morgan, J. P., Hort, M., Rüpke, L. H., 2011. 2D and 3D numerical models on compositionally buoyant diapirs in the mantle wedge. Earth and Planetary Science Letters 311 (1), 53–68.

Hashiguchi, K., Yamakawa, Y., 2012. Introduction to finite strain theory for continuum elasto-plasticity. John Wiley & Sons.

Heister, T., Dannberg, J., Gassmöller, R., Bangerth, W., 2017. High accuracy mantle convection simulation through modern numerical methods–ii: realistic models and problems. Geophysical Journal International 210 (2), 833–851.

Hestenes, M. R., 1969. Multiplier and gradient methods. Journal of optimization theory and applications 4 (5), 303–320.

Hirth, G., Kohlstedt, D., 2003. Rheology of the upper mantle and the mantle wedge: A view from the experimentalists. Inside the subduction Factory, 83–105.

Hughes, T., 1987. The Finite Element Method: linear static and dynamic finite element analysis, 1st Edition. Englewood Cliffs: Prentice-Hall.

Jarvis, G. T., McKenzie, D. P., 1980. Convection in a compressible fluid with infinite Prandtl number. Journal of Fluid Mechanics 96 (3), 515–583.

Karato, S.-i., Riedel, M. R., Yuen, D. A., 2001. Rheological structure and deformation of subducted slabs in the mantle transition zone: implications for mantle circulation and deep earthquakes. Physics of the Earth and Planetary Interiors 127 (1), 83–108.

Kaus, B. J., mar 2010. Factors that control the angle of shear bands in geodynamic numerical models of brittle deformation. Tectonophysics 484 (1-4), 36–47.

King, S. D., Lee, C., Van Keken, P. E., Leng, W., Zhong, S., Tan, E., Tosi, N., Kameyama, M. C., 2010. A community benchmark for 2-d cartesian compressible convection in the earth's mantle. Geophysical Journal International 180 (1), 73–87.

Kronbichler, M., Heister, T., Bangerth, W., 2012. High accuracy mantle convection simulation through modern numerical methods. Geophysical Journal International 191 (1), 12–29.

Maday, Y., Patera, A. T., 1989. Spectral element methods for the incompressible navier-stokes equations. In: IN: State-of-the-art surveys on computational mechanics (A90-47176 21-64). New York, American Society of Mechanical Engineers, 1989, p. 71-143. Research supported by DARPA. pp. 71–143.

Maffione, M., Thieulot, C., Van Hinsbergen, D. J., Morris, A., Plümper, O., Spakman, W., 2015. Dynamics of intraoceanic subduction initiation: 1. oceanic detachment fault inversion and the formation of supra-subduction zone ophiolites. Geochemistry, Geophysics, Geosystems 16 (6), 1753–1770.

Moresi, L., Dufour, F., Mühlhaus, H.-B., 2003. A Lagrangian integration point Finite Element Eethod for large deformation modeling of viscoelastic geomaterials. Journal of Computational Physics 184 (2), 476–497.

Morgan, J. P., 2001. The role of serpentinization and serpentinization in bending and unbending the subducting slab. AGU 82, F1154.

Muskhelishvili, N., 1953. Some Basic Problems Of The Mathematical Theory Of Elasticity. Oxford University Press, Bombay.

Petrunin, A., Sobolev, S. V., 2006. What controls thickness of sediments and lithospheric deformation at a pull-apart basin? Geology 34 (5), 389–392. URL `http://geology.gsapubs.org/content/34/5/389.abstract`

Poirier, J.-P., 1985. Creep of crystals: high-temperature deformation processes in metals, ceramics and minerals. Cambridge University Press.

Popov, A. A., Sobolev, S. V., 2008. SLIM3D: A tool for three-dimensional thermomechanical modeling of lithospheric deformation with elasto-visco-plastic rheology. Physics of the Earth and Planetary Interiors 171 (1-4), 55–75.

Powell, M. J., 1967. " A method for non-linear constraints in minimization problems". UKAEA.

Quareni, F., Yuen, D. A., Saari, M. R., 1986. Adiabaticity and viscosity in deep mantle convection. Geophysical Research Letters 13 (1), 38–41.

Quinteros, J., Ramos, V. a., Jacovkis, P. M., 2009. An elasto-visco-plastic model using the Finite Element Method for crustal and lithospheric deformation. Journal of Geodynamics 48 (2), 83–94.

Revenaugh, J., Parsons, B., 1987. Dynamic topography and gravity anomalies for fluid layers whose viscosity varies exponentially with depth. Geophysical Journal International 90 (2), 349–368.

Rockafellar, R. T., 1974. Augmented lagrange multiplier functions and duality in nonconvex programming. SIAM Journal on Control 12 (2), 268–285.

Schmalholz, S., Podladchikov, Y., Schmid, D., 2001. A spectral/finite difference method for simulating large deformations of heterogeneous, viscoelastic materials. Geophysical Journal International 145 (1), 199–208.

Schmid, D. W., Podladchikov, Y. Y., 2003. Analytical solutions for deformable elliptical inclusions in general shear. Geophysical Journal International 155 (1), 269–288.

Shewchuk, J. R., 1996. Triangle: Engineering a 2d quality mesh generator and delaunay triangulator. In: Applied computational geometry towards geometric engineering. Springer, pp. 203–222.

Spiegel, E. A., Veronis, G., 1959. On the Boussinesq approximation for a compressible fluid. Astrophysical Journal 131, 442.

Suckale, J., Nave, J.-C., Hager, B. H., 2010. It takes three to tango: 1. simulating buoyancy-driven flow in the presence of large viscosity contrasts. Journal of Geophysical Research: Solid Earth 115 (B7).

Thielmann, M., May, D., Kaus, B., 2014. Discretization errors in the hybrid finite element particle-in-cell method. Pure and applied geophysics 171 (9), 2165–2184.

Turcotte, D. L., Schubert, G., 2014. Geodynamics. Cambridge University Press.

van Keken, P., King, S., Schmeling, H., Christensen, U., Neumeister, D., Doin, M.-P., 1997. A comparison of methods for the modeling of thermochemical convection. Journal of Geophysical Research: Solid Earth 102 (B10), 22477–22495.

von Tscharner, M., Schmalholz, S., 2015. A 3-D Lagrangian Finite Element algorithm with remeshing for simulating large-strain hydrodynamic instabilities in power law viscoelastic fluids. Geochemistry, Geophysics, Geosystems 16 (1), 215–245.

Yuen, D. A., Quareni, F., Hong, H.-J., 1987. Effects from equation of state and rheology in dissipative heating in compressible mantle convection. Nature 326 (6108), 67.

Zhong, S., 1996. Analytic solutions for stokes' flow with lateral variations in viscosity. Geophysical Journal International 124 (1), 18–28.

Zienkiewicz, O., 1985. Iterative method for constrained and mixed approximation. An inexpensive improvement of F.E.M. performance. Computer Methods in Applied Mechanics and Engineering 51, 3–29.

Zienkiewicz, O. C., Taylor, R. L., 2005. The Finite Element Method for Solid and Structural Mechanics, 6th Edition. Elsevier.

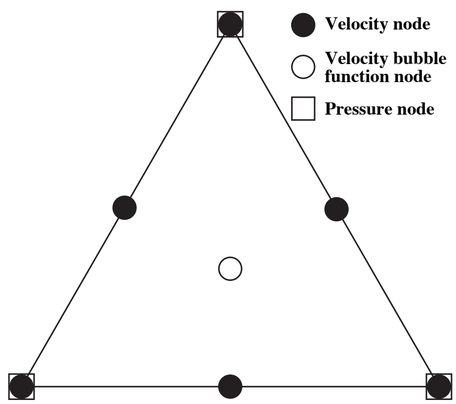

Figure .1: Crouzeix-Raviart triangular element. This element is characterised by continuous quadratic velocities with cubic bubble function in the barycenter of the triangle and discontinuous linear pressure and show quadratic convergence.

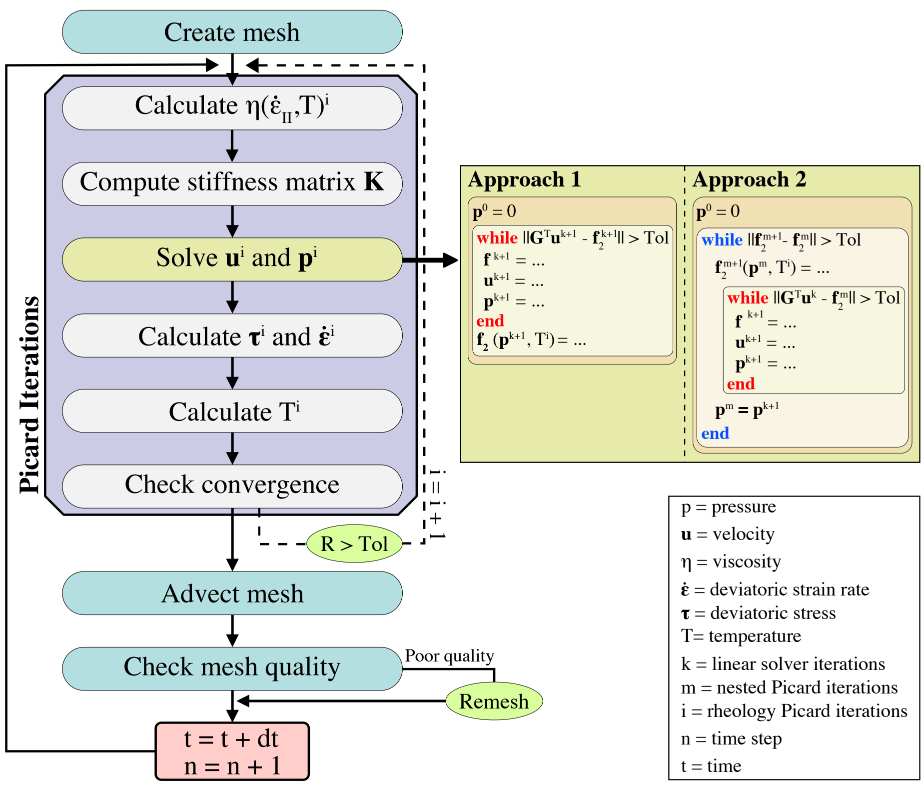

Figure .2: Global workflow of the code.

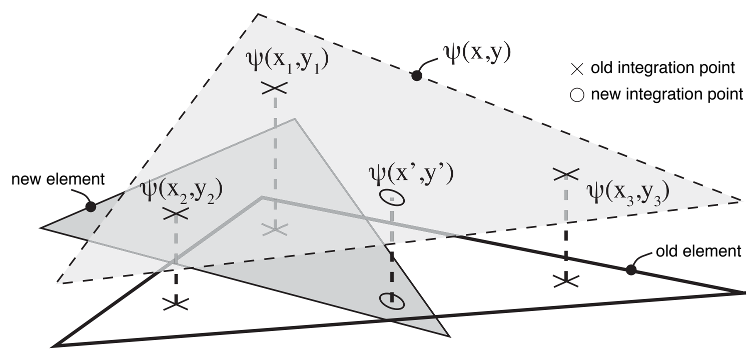

Figure .3: The information stored at the integration points of the elements of the old mesh is mapped onto the new elements using the shape functions as interpolation functions. For simplicity, the field $\Psi(x, y)$ depicted in this sketch is assumed to be linear.

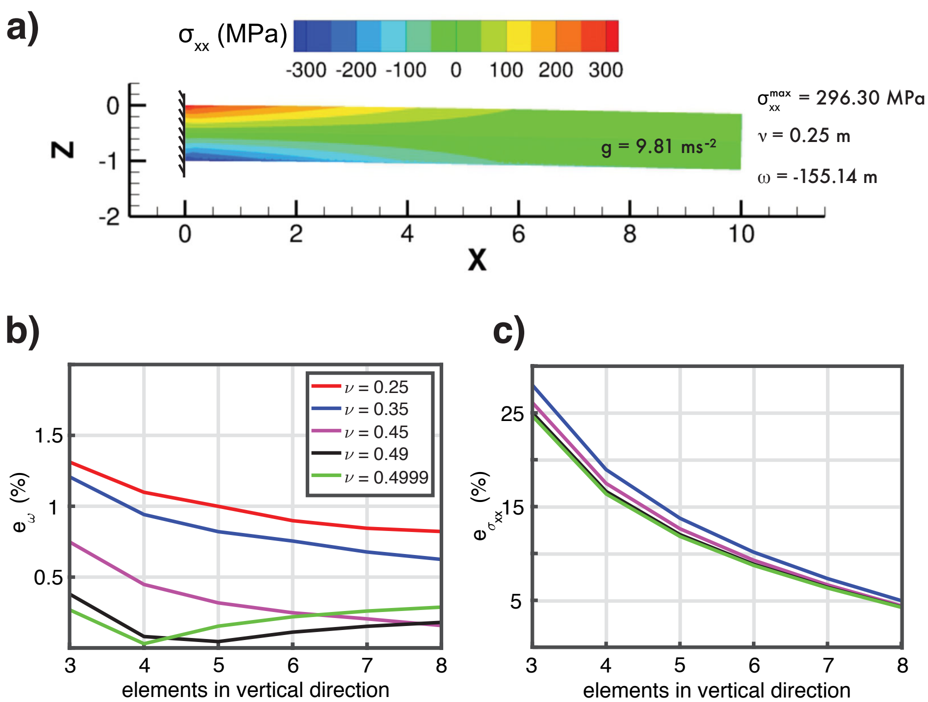

Figure .4: **a)** Set-up for the cantilever problem and flexure and stress field after loading for $\nu = 0.25$. **b)** and **c)**Relative errors of the maximum deflection and bending stress for a thin beam embedded in one side and subjected to a uniform loading.

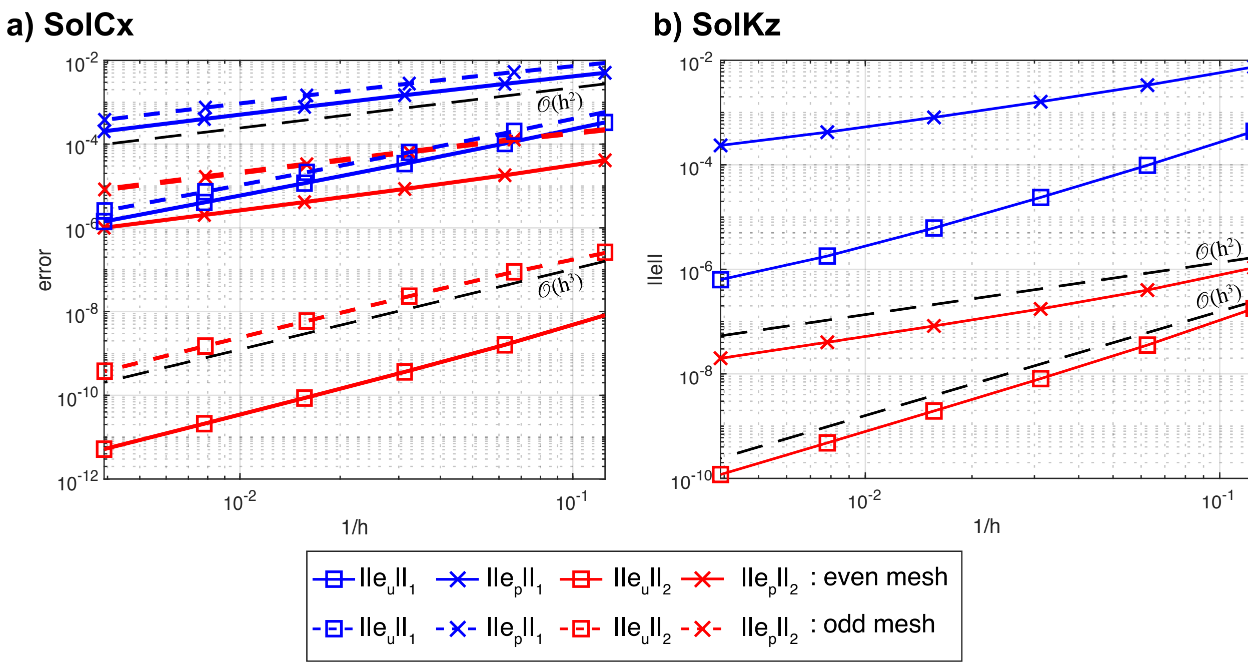

Figure .5: L_1 and L_2 norms for velocity and pressure with respect to the mesh resolution for the **a)** SolCx and **b)** SolKz tests.

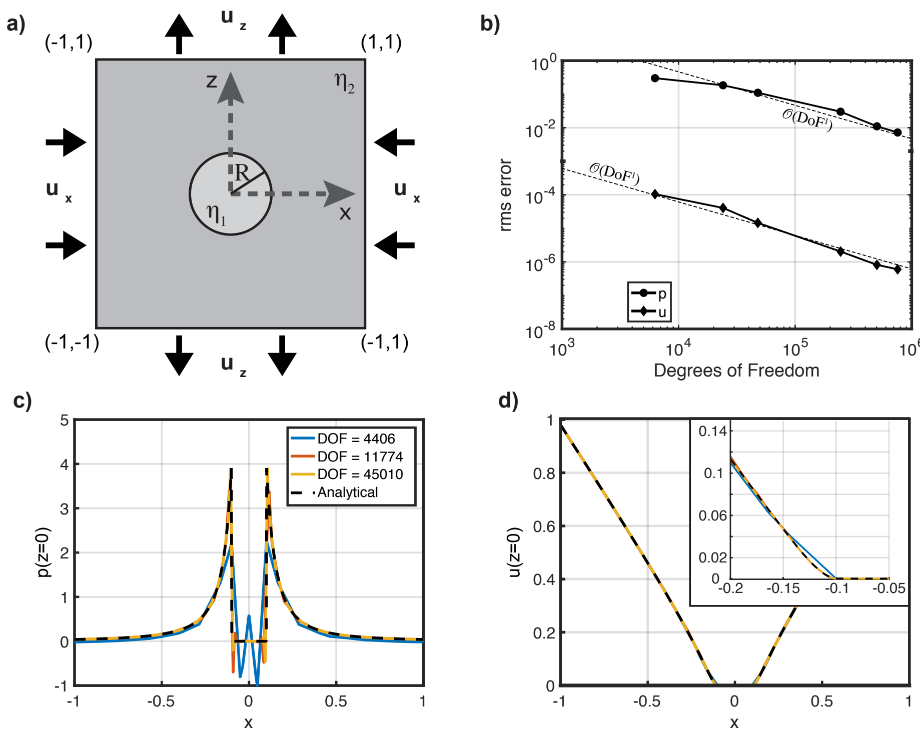

Figure .6: **a)** Set-up of a viscous inclusion within a homogeneous matrix. **b)** Pressure and velocity rms errors with increasing number of DoFs. Comparison of the analytical and numerical solutions along the plane $z = 0$ for the **c)** pressure and **d)** velocity fields. The inset in d) shows the smooth transition of the velocity field along the matrix-inclusion interface.

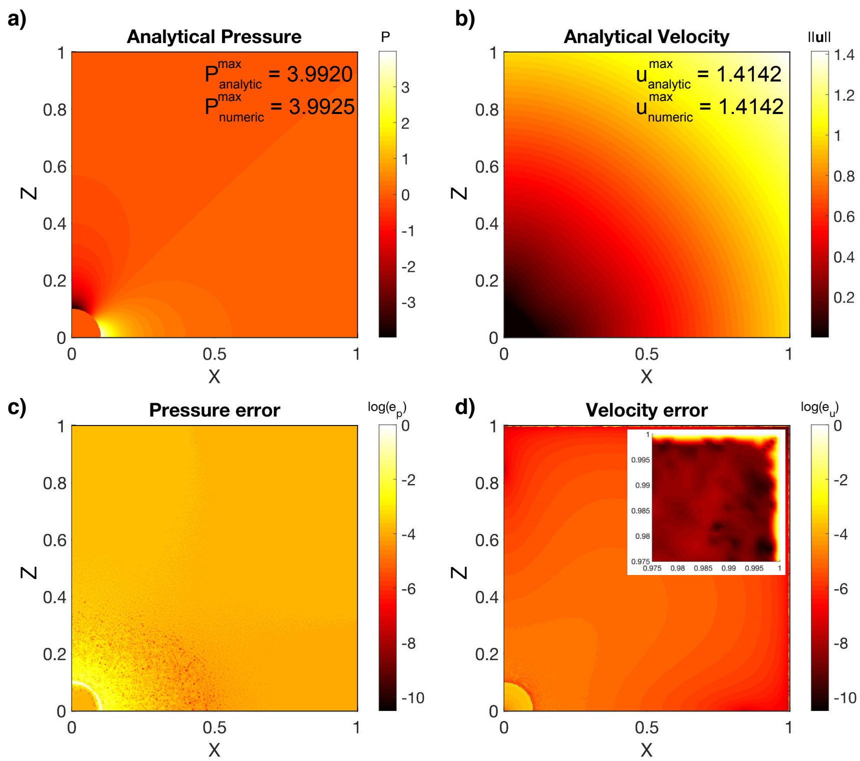

Figure .7: Analytical solutions of the **a)** pressure and **b)** velocity fields; and distribution of the logarithmic rms error of **c)** pressure and **d)** velocity. The zoom-in in d) shows the zero velocity error in the boundaries of the domain. Due to the symmetry of the pressure and velocity fields, only the upper-right corner of the domain ($\Omega' = [0, 1] \times [0, 1]$) is shown in this figure. The results shown here correspond to a mesh with $6.65 \cdot 10^5$ DOF. *Note*: as $log_{10}(0) \rightarrow -\infty$, values of $log_{10}(e_u = 0)$ are forced to be zero in panel **c**.

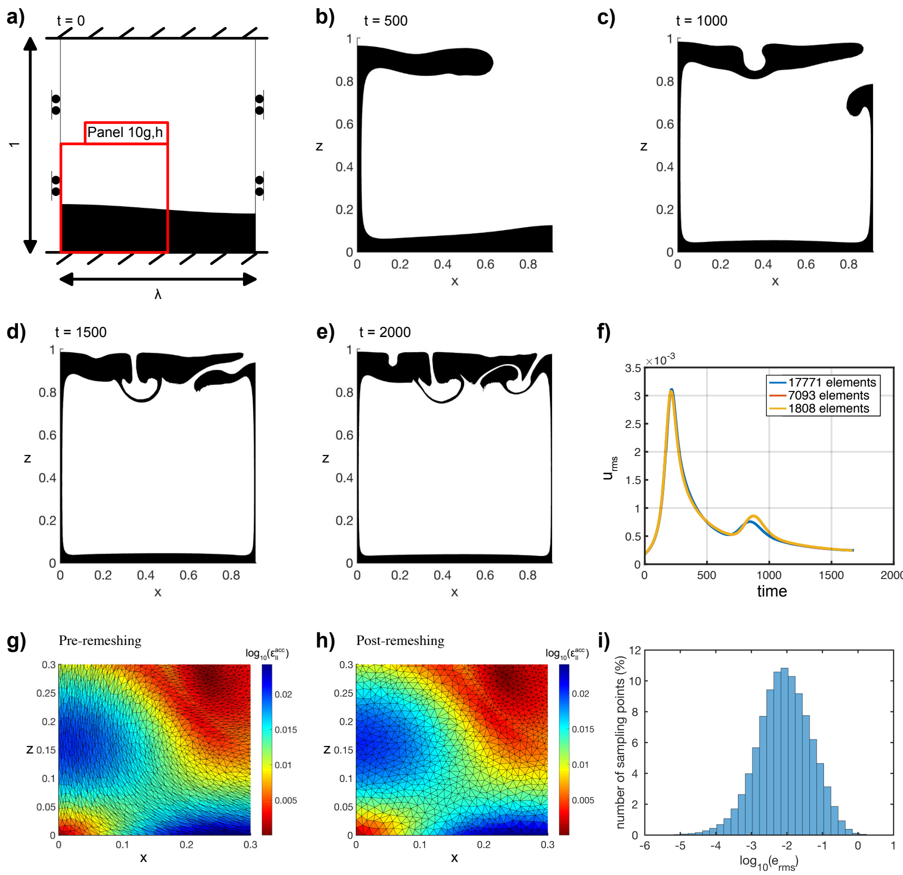

Figure .8: **a-e)** Temporal evolution of the Rayleigh-Taylor instability. **f)** Evolution of u_{rms}. Remeshing of the domain is necessary when the mesh becomes highly distorted. Note that the red lines overlap with the blue line. **g)** and **h)** Comparison between the second invariant of the accumulated strain ε_{II}^{acc} in a mesh with heavily distorted elements, and ε_{II}^{acc} interpolated into a new mesh. **i)** Histogram showing the logarithm of the error between the accumulated square root of second invariant of the strain rate, pre- and post-remeshing

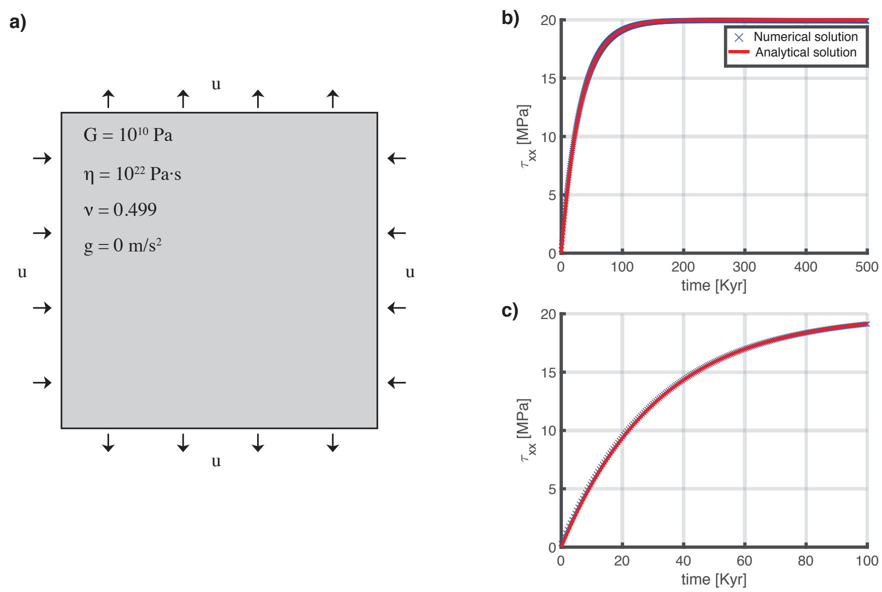

Figure .9: **a)** Set-up for the stress build-up experiment: a rectangular body is deformed with a constant background strain rate under pure shear boundary conditions. **b)** Comparison of the stress between the analytical solution and the numerical results. **c)** Zoom in the stress-time curve in the visco-elastic regime.

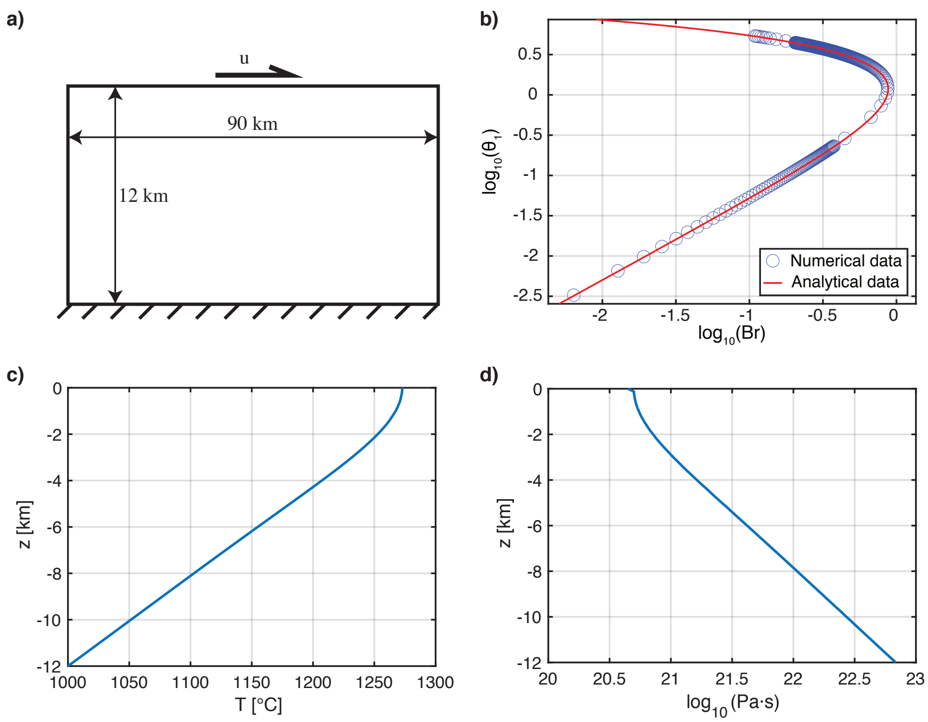

Figure .10: **a)** Set-up for Couette flow: the velocity at the bottom is u=0 and constant velocity u^* is prescribed at the top boundary. **b)** Analytical and numerical relationship between the Brinkman number and the non-dimensional temperature at the top of the Couette flow. Vertical **c)** temperature and **d)** viscosity profiles after $425 \cdot 10^3$ years.

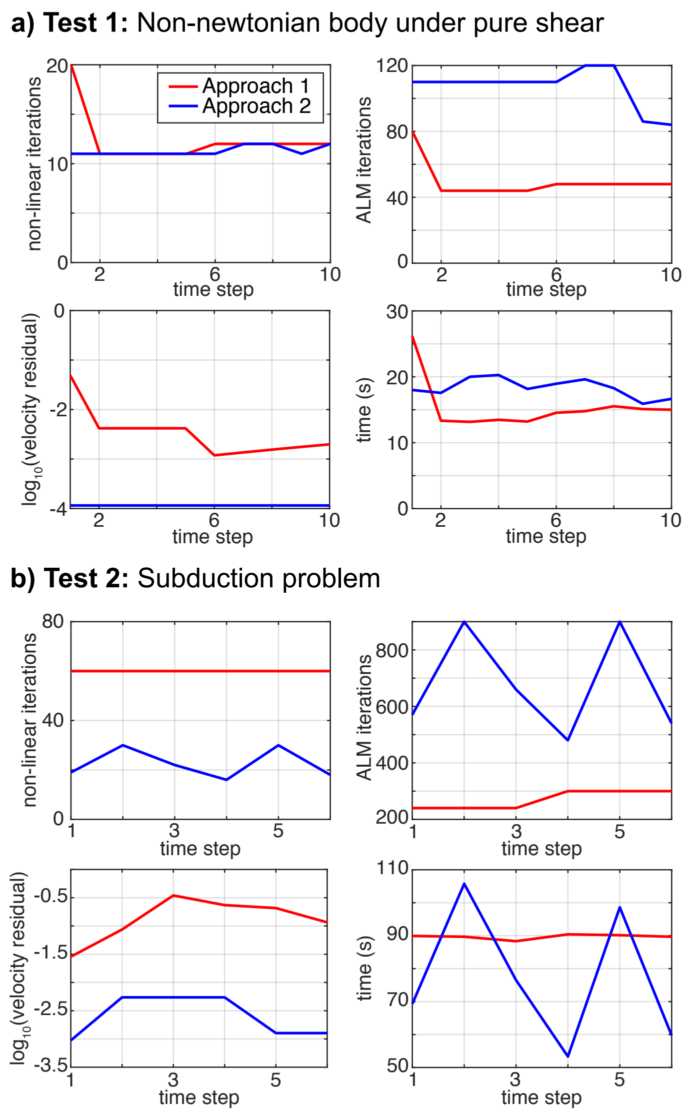

Figure .11: Comparison of the number of non-linear (upper left panel) and linear (ALM) iterations (upper right panel), residual velocity (lower left panel) and computational time (lower right panel)between Approach 1 and Approach 2 for **a)** Test A and **b)** Test B. The average computational times per time iteration for Test A are 15.43 s for Approach 1 and 18.34 s for Approach 2, whereas Test B yields average computational times of 89.68 s and 77.20 s for Approach 1 and 2, respectively.

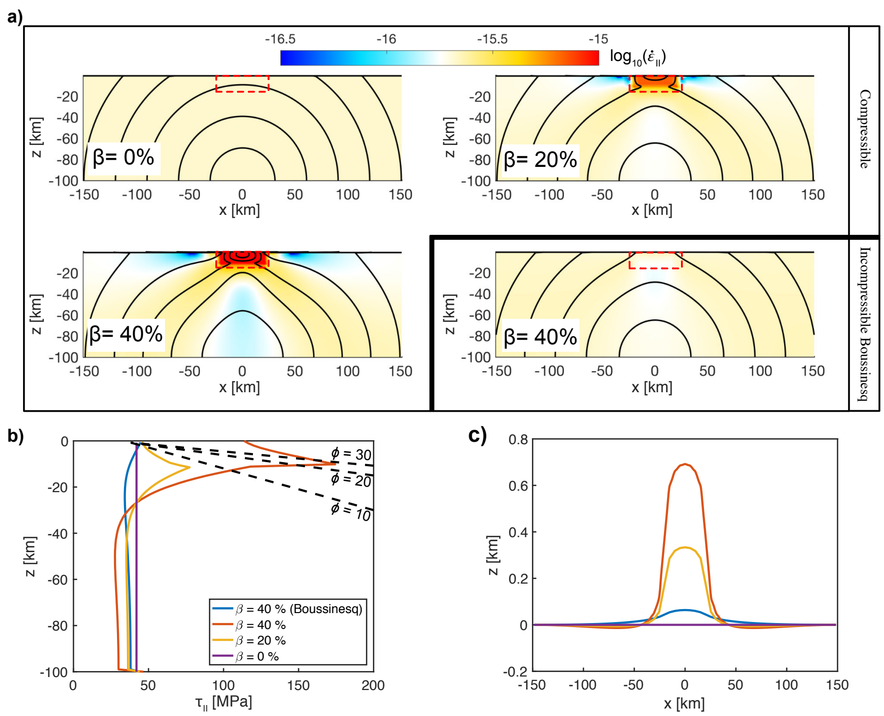

Figure .12: **a)** Results for different values of β. The density depends linearly on the degree of serpentinisation: $\beta = 0, 20$ and 40%. The color maps represent the square root of the second invariant of the stress and the thick black lines are isolines of the velocity field. The change of density occurs within the area delimited by the dashed red rectangle. **b)** Vertical profile of τ_{II} at x = 0; the dashed lines represent the yield stress given by a pressure dependent yield envelope: $\tau_y = p \sin\phi + C \cos\phi$, with C = 20 MPa. **c)** Comparison of the topographic relief for different degrees of serpentinisation. All the results shown here correspond to $t = 1$ Myr.

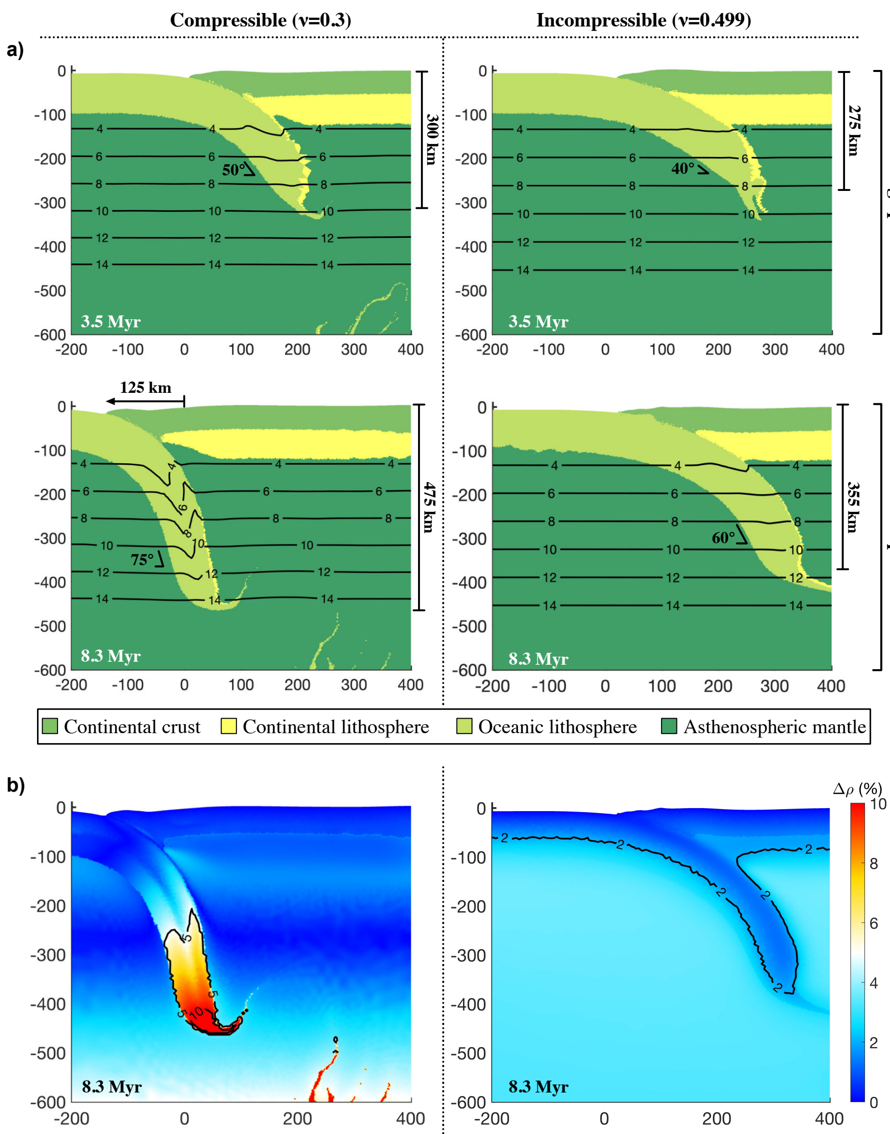

Figure .13: **a)** Snapshots of the subducting slab at 3.5 and 8.3 Myr for compressible ($\nu = 0.3$) and near-incompressible materials ($\nu = 0.499$). The solid black lines represents total pressure isolines, in GPa. **b)** Density variations, in absolute value, with respect to the reference state at 8.3 Myr. The "fingers" at the bottom of the compressible slab at 8.3 Myr are material that has been removed from the tip of the slab.

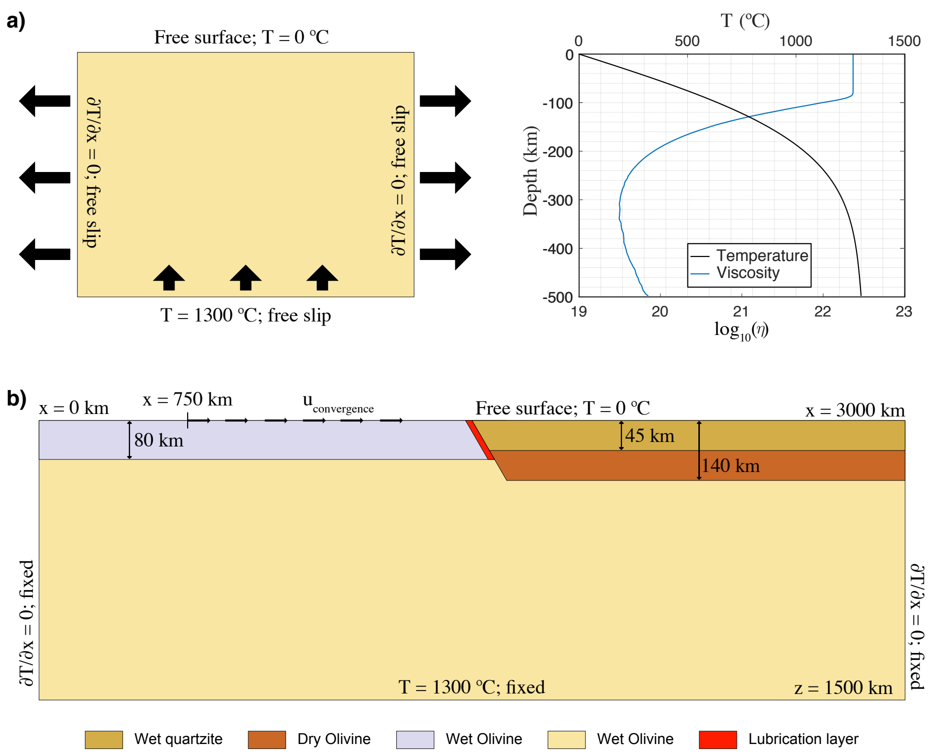

Figure .14: **a)** Model set-up, boundary conditions and vertical temperature and viscosity profiles of Test A. **b)** Model set-up and boundary conditions of Test B.

Table .1: Values of growth rate, maximum rms velocity and its corresponding time, obtained with an unstructured mesh of Crouzeix-Raviart elements. with respect to the methods HS, CND, SNK, and PvK presented in van Keken et al. (1997). The results are also in agreement with repetitions of this test employing more modern techniques, e.g. DynEarth2D (Choi et al., 2013), and "level sets" (Suckale et al., 2010)

Code	Elements (DOF)	γ	u_{rms}^{max}	t^{max}
LaCoDe (this study)	1808 (10754)	0.01221	0.003110	215
	7093 (2592)	0.01222	0.003080	212
	17960 (107468)	0.01222	0.003075	211
HS	81×81	0.01177	0.0030916	208.99
CND	48×48	0.01106	0.0030943	208.5
SK	160×160	0.01220	0.0028970	207.84
PvK	80×80	0.01225	0.003091	207.84
DynEarth2D	-	-	0.003106	215.25
Level sets	120×132	0.01252	0.00301	211.2

Table .2: Rheological parameters. Wet quartzite from Gleason and Tullis (1995) and dry olivine and wet olivine from Hirth and Kohlstedt (2003), respectively.

Parameter	Units	Wet Olivine	Dry Olivine	Wet Quartzite
c	MPa	20	20	20
ρ	kgm^{-3}	3300	3300	2850
G	GPa	74	74	36
α	-	$3 \cdot 10^{-5}$	$3 \cdot 10^{-5}$	$2.4 \cdot 10^{-5}$
H_Q	Wm^{-3}	0	0	$0.2 \cdot 10^{6}$
K	$Wm^{-3}K^{-3}$	3.3	3.3	2.5
$log_{10}(A)$	$Pa^{-n}s^{-1}$	-15.56	-15.56	-28
E	$KJmol^{-3}$	480	530	223
$log_{10}(V_o)$	m^3mol^{-3}	-6	-6	1
n_{dis}	-	3.5	3.5	4
n_{dif}	-	1	1	0